

University of Central Florida

**STARS**

---

Electronic Theses and Dissertations

---

2019

## Hybrid Integration of Second- and Third-order Highly Nonlinear Waveguides on Silicon Substrates

Guillermo Fernando Camacho Gonzalez  
*University of Central Florida*



Part of the [Electromagnetics and Photonics Commons](#), and the [Optics Commons](#)

Find similar works at: <https://stars.library.ucf.edu/etd>

University of Central Florida Libraries <http://library.ucf.edu>

This Doctoral Dissertation (Open Access) is brought to you for free and open access by STARS. It has been accepted for inclusion in Electronic Theses and Dissertations by an authorized administrator of STARS. For more information, please contact [STARS@ucf.edu](mailto:STARS@ucf.edu).

---

### STARS Citation

Camacho Gonzalez, Guillermo Fernando, "Hybrid Integration of Second- and Third-order Highly Nonlinear Waveguides on Silicon Substrates" (2019). *Electronic Theses and Dissertations*. 6459.  
<https://stars.library.ucf.edu/etd/6459>

HYBRID INTEGRATION OF SECOND- AND THIRD-ORDER HIGHLY NONLINEAR  
WAVEGUIDES ON SILICON SUBSTRATES

by

GUILLERMO FERNANDO CAMACHO GONZALEZ

B.S.Phys. Universidad Autonoma del Estado de Mexico, 2011

M.S. Instituto Nacional de Astrofisica, Optica y Electronica, 2015

A dissertation submitted in partial fulfillment of the requirements  
for the degree of Doctor of Philosophy  
in the College of Optics and Photonics  
at the University of Central Florida  
Orlando, Florida

Summer Term

2019

Major Professor: Sasan Fathpour

© 2019 Guillermo Fernando Camacho Gonzalez

## **ABSTRACT**

In order to extend the capabilities and applications of silicon photonics, other materials and compatible technologies have been developed and integrated on silicon substrates. A particular class of integrable materials are those with high second- and third-order nonlinear optical properties. This work presents contributions made to nonlinear integrated photonics on silicon substrates, including chalcogenide waveguides for over an octave supercontinuum generation, and rib-loaded thin-film lithium niobate waveguides for highly efficient second-harmonic generation. Through the pursuit of hybrid integration of the two types of waveguides for applications such as on-chip self-referenced optical frequency combs, we have experimentally demonstrated fabrication integrability of chalcogenide and thin-film lithium niobate waveguides in a single chip and a pathway for both second- and third-order nonlinearities occurring therein. Accordingly, design specifications for an efficient nonlinear integrated waveguide are reported, showing over an octave supercontinuum generation and frequency selectivity for second-harmonic generation, enabling potentials of on-chip interferometry techniques for carrier-envelope offset detection, and hence stabilized optical combs.

To my family, friends and mentors.

## **ACKNOWLEDGMENTS**

I thank my advisor, Dr. Sasan Fathpour, for his mentorship and his example of excellence.

I thank my colleagues, Ashutosh Rao, Marcin Malinowski, Amirmahdi Honardoost, Chih-Hao Li, Kamal Khalil, Tracy Sjaardema and Saeed Khan for their valuable support and friendship.

Special thanks to my family for their endless love and support.

# TABLE OF CONTENTS

LIST OF FIGURES.....	ix
LIST OF TABLES.....	xiii
CHAPTER 1: INTRODUCTION.....	1
CHAPTER 2: CHALCOGENIDE WAVEGUIDES.....	7
2.1 Introduction.....	7
2.2 Chalcogenide waveguides .....	8
2.3 Chalcogenide ring resonators.....	10
2.4 Supercontinuum in chalcogenide waveguides.....	14
2.4.1 Simulations.....	15
2.4.2 Fabrication.....	17
2.4.3 Measurements and results.....	18
2.5 2D Coupling tapers.....	19
CHAPTER 3: SECOND-HARMONIC GENERATION IN LITHIUM NIOBATE WAVEGUIDES..	23
3.1 Introduction.....	23
3.2 Phase matching in second-order nonlinear media.....	23
3.3 Thin film periodically poled lithium niobate.....	27

3.4	Mode-shape modulation on thin film lithium niobate.....	30
CHAPTER 4: HYBRID INTEGRATION OF CHALCOGENIDE AND LITHIUM NIOBATE		
WAVEGUIDES.....		
		32
4.1	Introduction.....	32
4.2	Integrability demonstration.....	35
4.2.1	Simulations.....	35
4.2.2	Fabrication.....	37
4.2.3	Measurements and results.....	38
4.3	Efficient supercontinuum in hybrid nonlinear waveguides.....	45
4.3.1	Precepts of the hybrid platform for high-performance cascaded nonlinearities .....	47
4.3.2	Dispersion calculations .....	49
4.3.3	Supercontinuum simulation.....	54
4.3.4	Fabrication.....	59
CHAPTER 5: FUTURE WORK .....		
		62
CHAPTER 6: CONCLUSION .....		
		65
APPENDIX A- FABRICATION METHODOLOGY.....		
		67
APPENDIX B-MATLAB CODES .....		
		71

APPENDIX C-COPYRIGHT PERMISSIONS ..... 78

LIST OF REFERENCES ..... 81

## LIST OF FIGURES

Figure 1: Bit rate-product evolution in time, solid circles represent the emerging of new technologies. Image from [4].....	2
Figure 2: $\text{Ge}_{23}\text{Sb}_7\text{S}_{70}$ chalcogenide dispersion (blue) and loss (green). Figure reproduced from [31]. © Nature publishing group.....	9
Figure 3: Fabrication process of chalcogenide waveguides. Special considerations are taken in steps 3 and 6, in order to protect the material and relieve stress issues. ....	9
Figure 4: a) Top view of the all-pass ring resonator waveguide. b) Transversal view of the fabricated ring. c) Optical mode distribution and effective refractive index for the ring, calculated with COMSOL.....	12
Figure 5: Numerical fitting to the measured ring resonances with a gap of 350 nm. For the resulting $Q = 10,835$ , the corresponding propagation loss is of 3.8 dB/cm. ....	13
Figure 6: SEM image of the waveguides, showing decent smooth sidewalls. ....	14
Figure 7: TE dispersion for chalcogenide waveguide with a $\text{SiO}_2$ slot, 1.5 $\mu\text{m}$ width, 1.225 $\mu\text{m}$ total height with a 125 nm slot at 760 height. ....	16
Figure 8: TE and TM dispersion lines for chalcogenide waveguide of 2.8 $\mu\text{m}$ width and 0.95 $\mu\text{m}$ height embedded in silicon dioxide.....	17

Figure 9: SC spectrum measures for the  $2.8 \times 0.95 \mu\text{m}^2$  chalcogenide waveguide. The orange plot correspond to the measurement of a short wavelength OSA, whereas the blue to a long wavelength OSA..... 19

Figure 10: Mode simulations for different cross sections along non inverted taper on chalcogenide ridge waveguides, overlap is shown for butt coupled light coming from a tapered fiber and the structure composition is shown in the lower right corner. ....20

Figure 11: 3D Visual representation of the overlap between the optical mode coming from the fiber and the 2D taper input area.....21

Figure 12: (a) Measured supercontinuum in ChG waveguides with non-inverted 2D tapers. (b) 3D schematic of the actual device.....22

Figure 13: a) SHG efficiency through propagation length, for different phase difference conditions. We call it coherence length  $L_c$ , to the length where maximum efficiency happens. Image from [37].....26

Figure 14: a) Periodically polled lithium niobate waveguide example, period can be designed to fulfill phase match condition of the required wavelength. b) Clear second harmonic signal at around 788 nm detected by an optical spectral analyzer. Results published in [26].....28

Figure 15: SHG for a 1950 nm pump, using a periodically poled lithium niobate waveguide, generating a converted signal at 973.2 nm. Results published in [38].....29

Figure 16: a) Mode-shape modulated rib on lithium niobate waveguide, period can be designed to fulfill phase match condition of the required wavelength. b) Second harmonic signal at around 784 nm detected by an optical spectral analyzer. Results published in reference [25].....31

Figure 17: Schematic of the integrated ChG-LN as well as the reference waveguides. Optical mode profiles of the structure are also shown for fundamental TE input at 1550 nm for different cross-sections. Adiabatic mode transition is shown in the inset. ....36

Figure 18: Coupling efficiency of the mode-converting tapers vs. (a) Length of the taper, (b) Different wavelengths, (c) The width of the taper’s tip, and (d) Misalignment between the centers of the ChG waveguide/taper and Si<sub>3</sub>N<sub>4</sub>-LN waveguide.....37

Figure 19: (a) Optical spectrum of output power for integrated as well as the reference waveguides for both TE and TM input polarization for 1490-1630 nm wavelength range, and (b) Optical spectrum of output power difference integrated and reference waveguides for TE and TM input polarization for 1550-1560 nm wavelength range. ....39

Figure 20: Schematic of the experimental setup for wavelength conversion via FWM. PC: Polarization Controller, EDFA: Erbium-doped fiber amplifier, OSA: Optical spectrum analyzer.....40

Figure 21: Bit rate-product evolution in time, solid circles represent the emerging of new technologies. Image from [4].....42

Figure 22: a) Evolution of pumps and converted signals with propagation. b) Comparison between measured and numerically calculated conversion at different input powers.....43

Figure 23: Detailed mode analysis showing how the inflection points of the GVD arise when the mode is expanded into adjacent regions for the TE polarization. TM dispersion is also shown for comparison..... 52

Figure 24: Dispersion plots for the ChG waveguide by (a) height and (b) width variations. The continuous line in green represents the chosen dispersion for SCG..... 53

Figure 25: Pulse evolution in wavelength (a) and time (b) domains, after 40 mm propagation of TE modes in hybrid ChG waveguides. It is evident how the pulse starts braking in the time domain after 15 mm, progressing to high compression at 20 mm. The supercontinuum finally extends from ~1150 to > 2800 nm at 20 dB below maximum, i.e., over 1.25 octave..... 58

Figure 26: (a) Quasi-TE optical mode being coupled from ChG to LN; (b) Fundamental mode distribution in ChG waveguide; (c) Fully integrated nonlinear chip for cascaded  $\chi^{(2)}$  and  $\chi^{(3)}$  effects; (d) Coupling efficiency through a sweep of taper lengths; (e) Fundamental mode distribution in LN waveguide. .... 60

Figure 27: Top view and side view of the proposed fully integrated nonlinear chip, which includes a ChG channel waveguide for supercontinuum, beam splitters and PPLN [80]. 64

## LIST OF TABLES

Table 1 Sellmeier coefficients for the materials involved in the nonlinear chip integration  
[31, 70, 71, 72].  $n_{2\lambda} = A + B_1\lambda^2\lambda^2 - C_1 + B_2\lambda^2\lambda^2 - C_2 + B_3\lambda^2\lambda^2 - C_3$ .....50

## CHAPTER 1: INTRODUCTION

The phenomenon of light being guided within cavities through total internal reflection was first demonstrated in 1841 by Jean-Daniel Colladon [1, 2]. However, it was not until the 1960s when, among others, Charles K. Kao, a Nobel Prize Laureate, found a life-changing application for it. He pioneered the use of fiber-optic cables in telecommunications [3]. Along with the invention of lasers, it was a remarkable revolution in the history of telecommunications. With benefits such as wider bandwidth for data transmission and improved losses, in comparison to their copper counterpart, optical fibers came to replace copper wires in long-distance data transmission. A common figure of merit that help us to compare these technologies performance is the bit rate-distance product. In Figure 1 [4], we can see how optical fiber technologies have taken the largest steps in regard to this figure of merit.

In the beginning, optical fibers were passive devices that would only transmit light, so in order to apply this to telecommunications, it was necessary to develop the so-called active components, i.e., devices capable of controlling optical wave characteristics such as phase and amplitude for modulation and amplification.

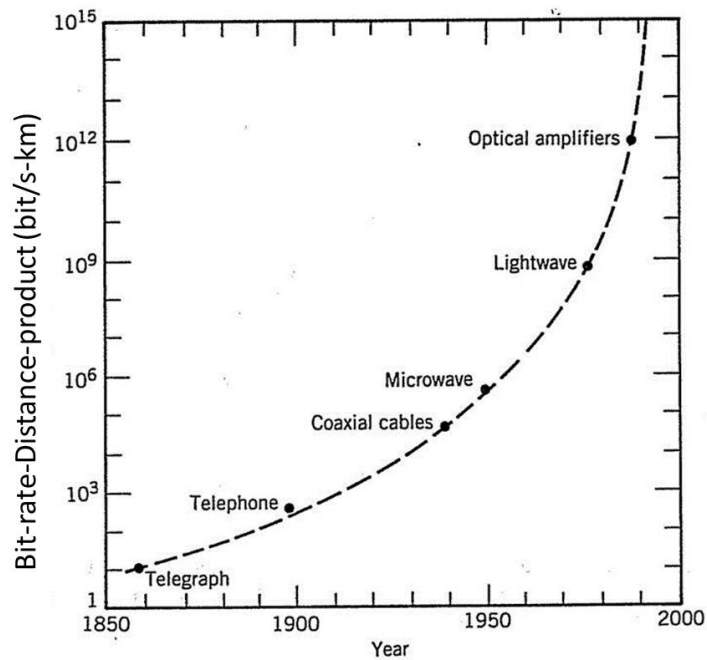


Figure 1: Bit rate-product evolution in time, solid circles represent the emerging of new technologies. Image from [4].

In homology, as optical fibers came to replace copper wires for data transmission, the field of integrated photonics emerged as an approach to replace data transmission in smaller scales, e.g., chip-to-chip communication within a computer motherboard. Integrated photonics is an analogy to integrated electronics, with the difference that photonics refers to the manipulation and control of light quanta "photons", whereas electronics refers to electric charge quanta "electrons".

Silicon is an excellent platform for integrated electronic circuits because of many advantages compared to other semiconductors, but especially because of its abundance on earth and feasible manipulation, which make it very inexpensive to the grade that

nowadays it is all around us in every electronic device we use in our daily life. Naturally, silicon is a desired candidate for integrated photonics, as well, having in mind its compatibility with Complementary Metal-Oxide-Semiconductor (CMOS) electronic circuits. In order to confine an optical mode within silicon waveguides, it must be surrounded by a lower index material, so we have to separate the guiding silicon layer from the silicon substrate. This challenge was solved with the development of silicon-on-insulator (SOI) wafers, which consist of a thick (substrate) and a thin (guiding) silicon layers, separated by a dielectric lower-index film, typically silicon dioxide ( $\text{SiO}_2$ ). Numerous papers have been published in the pursuit of silicon as the unifying material of integrated photonics and very good fabrication results are accomplished. Review of the field of silicon photonics can be found in several good review papers (e.g., [5, 6, 7, 8, 9, 10]).

Although integrated optics and electronics started their development around the same time, integrated photonics has over the decades developed at a considerably slower pace than integrated electronics, in integration density as well in total number of devices on a chip [11]. However, this situation has been changing recently by the effort and progress made by many research groups, in the field of heterogeneous integration of materials like III-V compound semiconductors (GaAs, InP systems, etc.), ferroelectric and piezoelectric materials with electro-optic effects (e.g.,  $\text{LiNbO}_3$  and AlN), dielectrics (e.g., SiN), glasses (e.g., chalcogenides), polymers, and many more on silicon substrates. Together with

emerging nanotechnologies, these developments have made integrated photonics solidly entrenched in a growing number of applications.

It can be argued that heterogeneous integration is pivotal to enhance the future of integrated photonics and its applications. Particularly, different materials can compensate for silicon's shortcomings when it comes to active photonic devices, especially at the infrared and telecom wavelengths, where shortcomings like two-photon absorption, free-carrier absorption, indirect bandgap for light generation, lack of second-order optical nonlinearity, etc., hamper the performance of SOI photonics [12].

My research group has contributed with the development of a variety of devices compatible with the CMOS technology, to mention some of the most relevant: Tunable delay lines were demonstrated on all-silicon chips [13, 14, 15, 16], silicon-on-nitride waveguides for mid-infrared operation [17], high-contrast silicon waveguides [18, 19, 20], thin-film LiNbO<sub>3</sub> on silicon for electro-optic and nonlinear applications [21, 22, 23, 24, 25, 26, 27], integrated polarization splitters with artificial anisotropic waveguides [28], chalcogenide waveguides for supercontinuum generation, etc. Ahead in this document, I describe in detail the works I have contributed to and how my interest in research is directed into a path of integration of different nonlinear materials, in order to combine the advantages offered by each of them, namely, LiNbO<sub>3</sub> with its characteristic strong second-order nonlinearity,  $\chi^{(2)}$ , and chalcogenide with strong third-order nonlinearity,  $\chi^{(3)}$ .

Carrier envelope offset (CEO) detection through  $f$ -to- $2f$  interferometry, is an application that seems directly benefitted by the hybrid nonlinear integration. It consists of the interference of a second harmonic converted signal from a comb spectrum, with its closer frequency, all within the comb. This two-wave interference produces a beat note which frequency belongs to the microwave regime, making it straight forward to measure it by simply using a conventional fast photodetector. Therefore, it is necessary to generate a comb of at least two octaves spanning. The necessary octave frequency comb can be obtained by supercontinuum generation in chalcogenide, and second harmonic generation can be efficiently generated in the lithium niobate waveguides. The integration of these two waveguides on a single chip can lead to on-chip CEO detection. The detected signal can be used as feedback for stabilization of the frequency comb, which is a significant step towards many important applications in various fields within chemistry, biology and physics.

In chapter 2 of this dissertation, I start presenting the work developed in chalcogenide waveguides. This chapter will help the reader to understand what a chalcogenide is and make him familiar with the concept of supercontinuum generation (SCG). Fabrication methods and fabricated devices are presented, including ring resonators, 2D coupling non-inverted tapers and supercontinuum waveguides.

Chapter 3 focuses on thin-film lithium-niobate developed technologies for second-order nonlinear processes enhancement, specifically second-harmonic generation (SHG). Two

different approaches for phase matching are discussed, namely, periodically poled lithium niobate and rib-loaded corrugated waveguides. Second harmonic measurement on these two technologies are presented at 1.5  $\mu\text{m}$  and 2  $\mu\text{m}$  pump wavelengths, along with a 2D coupling tapers design.

In chapter 4, hybrid integration ChG and LN waveguides is presented. We demonstrated integrability of the two materials in a fabricated chip. In this chapter you will find a more thorough description of the nonlinear processes that lead to SCG, and a careful design of an optimized hybrid waveguide for over an octave supercontinuum generation. This design is required to enable on-chip  $f$ -to- $2f$  carrier envelope offset detection.

We conclude with a summary and a general discussion of the hybrid nonlinear integration in chapter 5.

## CHAPTER 2: CHALCOGENIDE WAVEGUIDES

### 2.1 Introduction

Inducing nonlinear optical phenomena in integrated photonic devices is necessary to expand their functionality. The third order optical nonlinearity, also known as Kerr effect, can lead to an ultra-broad spectrum stretch of an input signal through various nonlinear processes, including self-phase modulation, cross-phase modulation, parametric four-wave mixing, soliton fission and modulation instability. Raman scattering is another nonlinear process that leads to spectrum broadening. A supercontinuum (SC) of light is generated when a narrowband pulse undergoes an extreme spectral broadening due to the above mentioned third-order nonlinear effects [29]. Low-loss materials and high nonlinearity are necessary to achieve broadband SC and fortunately both can be fulfilled by chalcogenide glasses (ChG) in the realm of telecom wavelengths. The particular ChG composition that we used is  $\text{Ge}_{23}\text{Sb}_7\text{S}_{70}$ . My first work, presented as a poster, was the design, fabrication and characterization of low-loss and broadband SC chalcogenide waveguides, which is going to be described ahead in this chapter.

In the following subsections, we start describing what chalcogenide is and the reasons why we consider it a suitable candidate for efficient SC generation. Subsequently, we discuss the fabrication considerations for ChG waveguides, followed by a detailed description of our ChG based developed technologies. This includes ring resonators for

waveguide loss characterization, supercontinuum waveguides and 2D tapered couplers for a reduction of the chip's insertion loss.

## 2.2 Chalcogenide waveguides

"Chalcogenide" is the name given to glasses, where an element from the group 16 in the periodic table (also known as chalcogens) other than oxygen (e.g., sulfur, tellurium or selenium), is combined with linking elements such as silicon, arsenic, germanium, phosphorus or antimony. The resulting glasses possess a high third order optical nonlinearity, compared to silicon nitride and other nonlinear candidates. The higher the concentration of the chalcogen in the mixture, the higher the nonlinearity, but it comes at the cost of robustness reduction. A high concentration of the chalcogen in the mixture, makes the glasses more susceptible to thermal changes, making it difficult to integrate with other standard waveguide materials.

The exact composition we used for our waveguides is  $\text{Ge}_{23}\text{Sb}_7\text{S}_{70}$ . Developed by L. Petit et al. [30], it has negligible loss at telecom wavelengths, a nonlinearity as high as  $n_2 = 3.71 \times 10^{-18} \text{m}^2/\text{W}$ , and has the advantage of low toxicity compared to its widely studied arsenic based competitor. The material bandgap falls around the 800 nm wavelength, which also results in negligible two photon absorption at 1.55  $\mu\text{m}$  pump wavelength, attributes that make it suitable for efficient nonlinear processes. Figure 2 shows the measured dispersion and absorption for the discussed material.

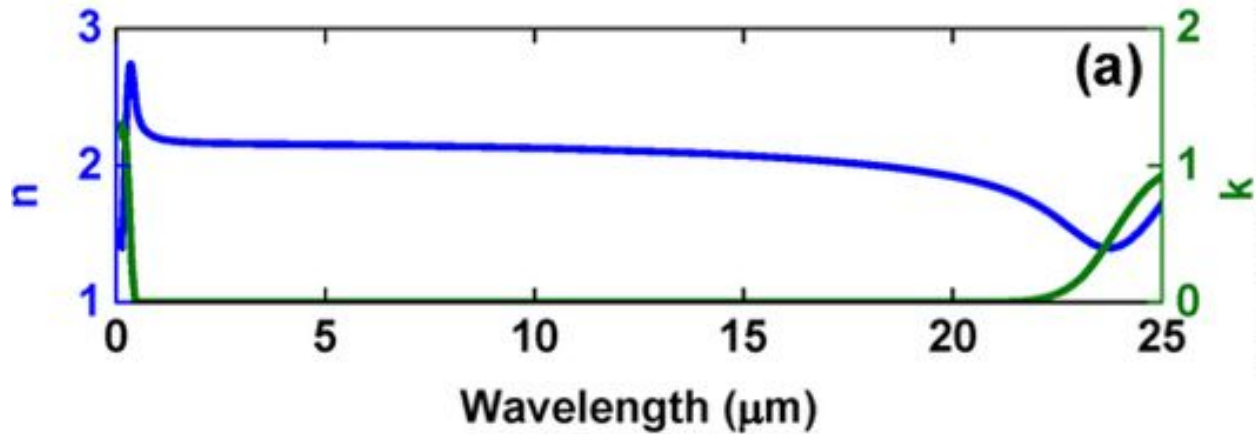


Figure 2:  $\text{Ge}_{23}\text{Sb}_7\text{S}_{70}$  chalcogenide dispersion (blue) and loss (green). Figure reproduced from [31]. © Nature publishing group.

A general drawback that arises with the large concentration of the chalcogen element in chalcogenide compositions, is the thermal expansion enhancement, which makes it challenging to integrate these glasses with other typical photonic materials. Thus, special considerations have to be taken when fabricating chalcogenide waveguides.

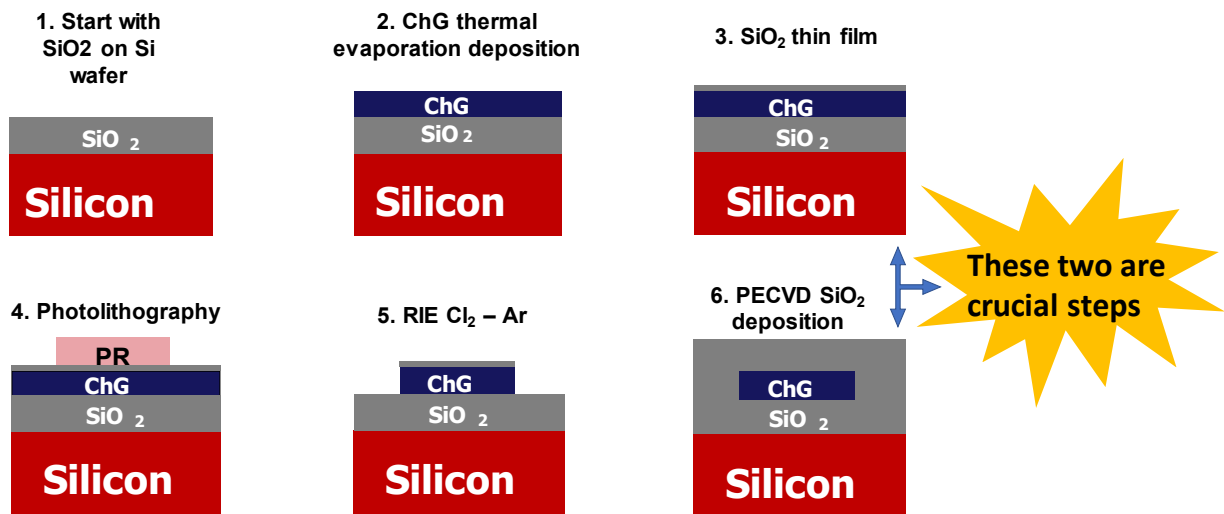


Figure 3: Fabrication process of chalcogenide waveguides. Special considerations are taken in steps 3 and 6, in order to protect the material and relieve stress issues.

The fabrication process we follow for the fabrication of chalcogenide waveguides is represented in Figure 3. We start with an oxidized silicon wafer, we deposit the chalcogenide thin layer by thermal evaporation, maintaining a rate around  $10 \text{ \AA/s}$  to ensure the quality of the film. During evaporation, a longer distance between the vaporizer boat and the sample leads to cleaner deposition and even distribution of the film, resulting in good flatness and low propagation losses. The deposited film is immediately protected with an ultra-thin film oxide deposition, either by sputtering or by plasma enhanced chemical vapor deposition (PECVD), for protection against unwanted chemical etch, caused by some photoresist developers that may attack chalcogenide. Conventional photolithography is next used to mask the film. We continue with the ChG etching, using our self-developed chlorine-argon based dry etch recipe. This recipe can be found with better detail in appendix A. The final step consists of simple silicon dioxide passivation, which develops less stress problems if the passivation film is deposited with sputtering, given that it is a cold deposition, however, better quality depositions are gotten with PECVD.

### **2.3 Chalcogenide ring resonators**

A ring resonator consists of a closed circuit optical waveguide, such that a resonance occurs when the optical path length matches exactly a whole number of wavelengths. In analogy to a Fabry-Perot cavity, ring resonators support multiple resonances, and the

spacing between them is the free spectral range (FSR), which depends on the resonator length as  $\Delta\lambda = \lambda^2/n_{eff}L$ , with  $n_{eff}$  the effective refractive index of the propagating mode in the waveguide, and  $L$  the total length of the ring. An additional open waveguide can be used to couple light into the ring resonator through evanescent field interaction. A ring resonator coupled to a single waveguide is called an "all-pass ring resonator", and can be used to characterize waveguide propagation losses through transmission measurement as

$$T_n = \frac{I_{pass}}{I_{input}} = \frac{a^2 - 2r\cos(\phi) + r^2}{1 - 2r\cos(\phi) + (ra)^2} \quad (1)$$

where the transmission is given by the intensity transmitted divided by the input intensity. In this equation,  $\phi$  is the total phase shift in the ring,  $r$  is the self-coupling coefficient,  $a$  represents the single-pass amplitude transmission, including both propagation loss in the ring and loss in the couplers. It relates to the power attenuation coefficient  $\alpha$  as:

$$a^2 = e^{-\alpha L} \quad (2)$$

We fabricated ChG rings of 300  $\mu\text{m}$  diameter, and varied the gap between the ring and the bus waveguide from 210 nm to 610 nm (Figure 4(a)). The transversal dimensions of the fully etched rings are depicted in Figure 4(b), with 700 nm wide by 800 nm tall. Figure 4(c) shows the optical mode distribution simulated using COMSOL multiphysics. The calculated effective refractive index is 1.85, which results in a calculated FSR of 0.0013  $\mu\text{m}$ .

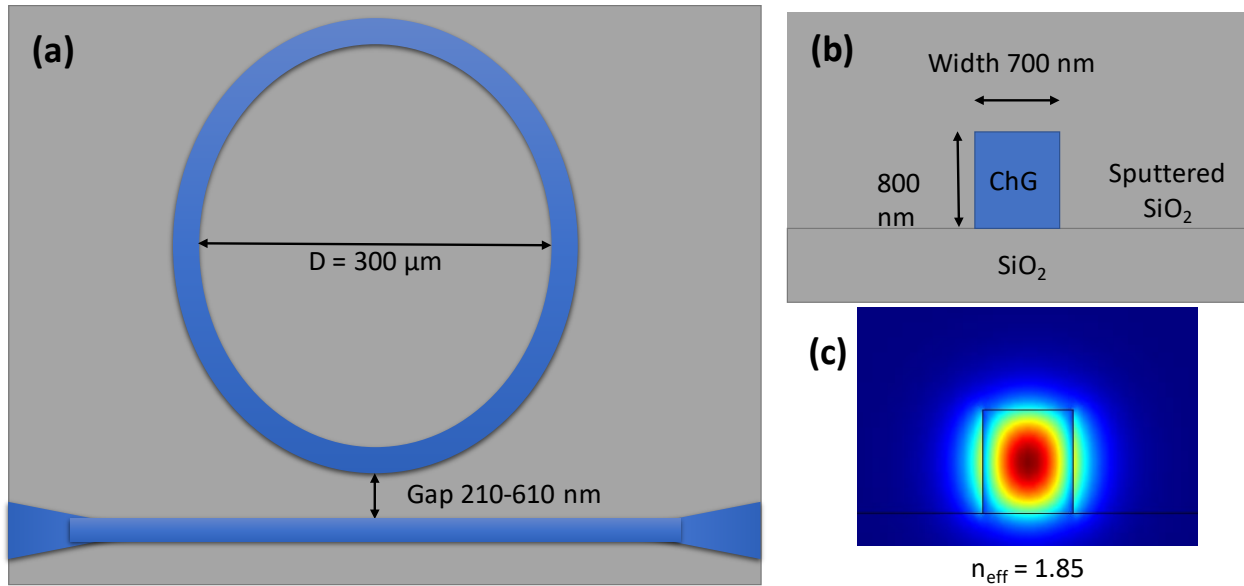


Figure 4: a) Top view of the all-pass ring resonator waveguide. b) Transversal view of the fabricated ring. c) Optical mode distribution and effective refractive index for the ring, calculated with COMSOL.

The transmission measurements for the best ring, with a gap of 350 nm, are presented in Figure 5, showing the measured data in blue, and the numerical fit in red. The experiment to get these measurements consists of a tunable laser, sweeping a certain span of waveguides at a selected speed, used as the input source. At the output we use a power-meter synchronized with the tunable laser, to finally get the transmission spectrum. By fitting equation (1) to the measurement, we can calculate numerically the values for  $Q$  and  $r$ , and thus, allowing us to calculate the waveguide propagation losses through equation (2). The resulting  $Q$  is 10,835, and the calculated propagation loss is 3.8 dB/cm.

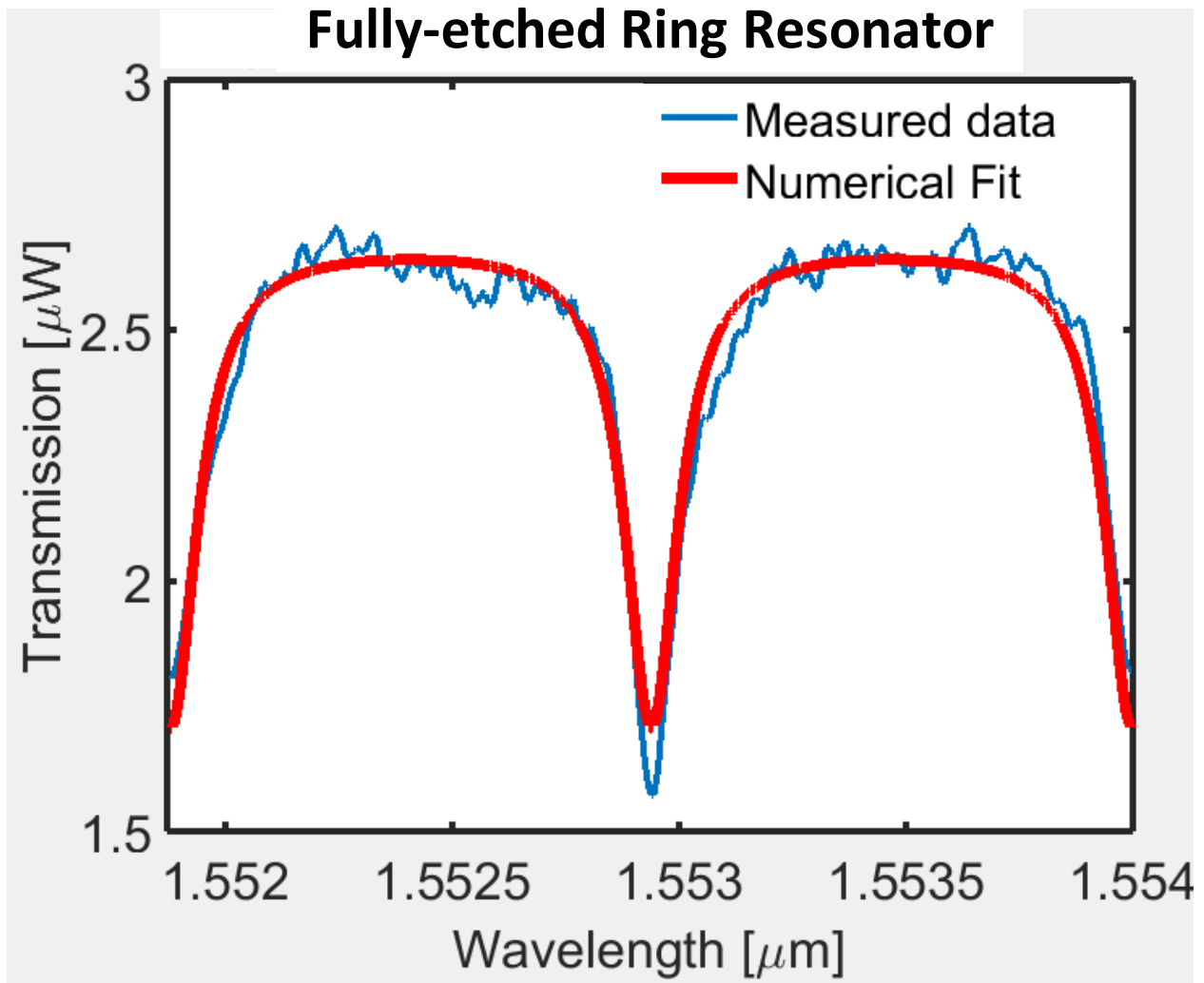


Figure 5: Numerical fitting to the measured ring resonances with a gap of 350 nm. For the resulting  $Q = 10,835$ , the corresponding propagation loss is of 3.8 dB/cm.

A scanning-electron microscope (SEM) was used to image the waveguides before cladding (Figure 6). We observe decent smoothness at the sidewalls. Another attempt of imaging was made after cladding the samples with sputtered oxide to study the material deposition at the sidewall, which is not significant enough to use the machine for anti-reflection coatings.

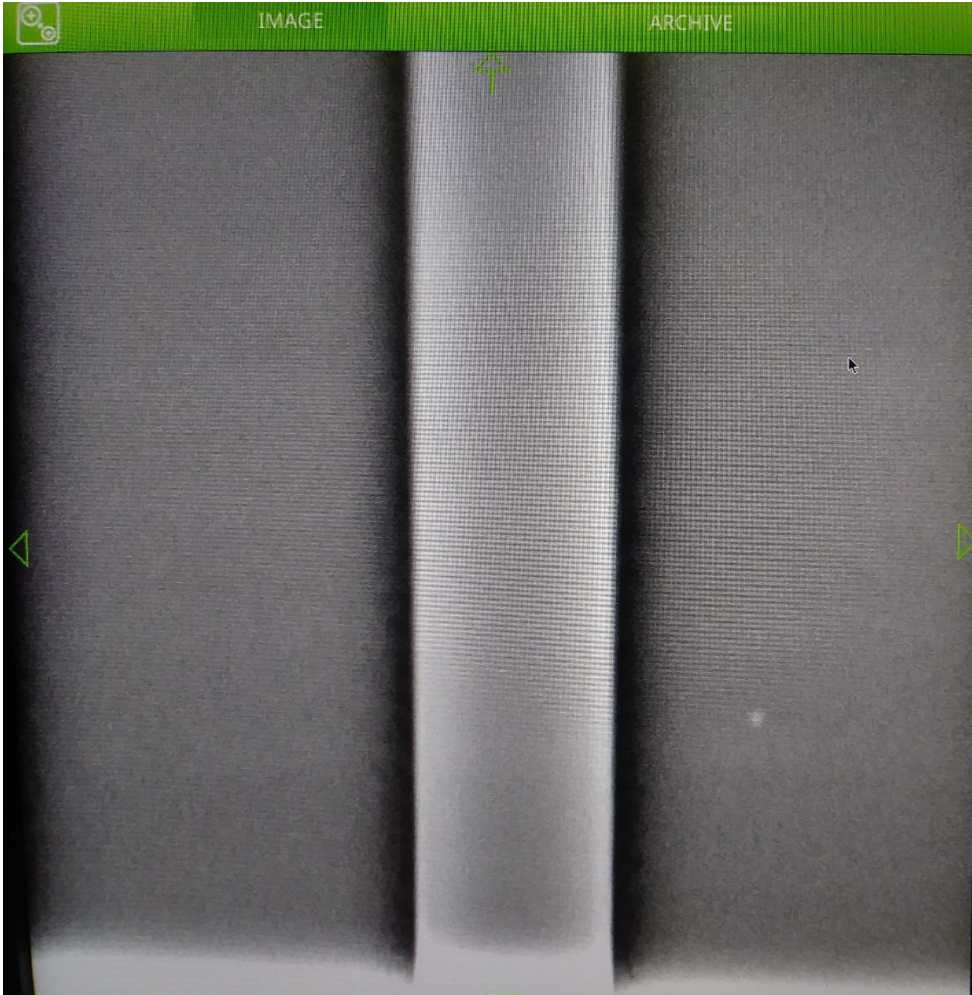


Figure 6: SEM image of the waveguides, showing decent smooth sidewalls.

## 2.4 Supercontinuum in chalcogenide waveguides

In this section, we study the requirements needed to successfully generate supercontinuum in chalcogenide waveguides. We go through all the fabrication process, from design to the final measurements of over an octave supercontinuum.

### 2.4.1 Simulations

A broad SC requires not only a highly nonlinear material, but a wide anomalous dispersion around the input wavelength, where the central input wavelength has a group velocity dispersion (GVD) as flat and close to zero as possible [32]. There are different methods to engineer dispersion in waveguides. Initially, we know that the total dispersion is a combination of material and waveguide dispersions, so without altering the material, the only way to change dispersion is to modify the waveguide dispersion. The straight forward method is to vary the cavity dimensions, one can also change the surrounding material index and a third, though not very straight forward method, is by adding a low index slot within the waveguide [33, 34, 35].

Figure 2a shows a four-zero dispersion I designed for a slot chalcogenide waveguide and the mode for different wavelengths. As we can see, the mode is contained into the slot at some point and this is not convenient because the interfaces are always lossy after fabrication and this way we would be losing a lot of the 2  $\mu\text{m}$  signal.

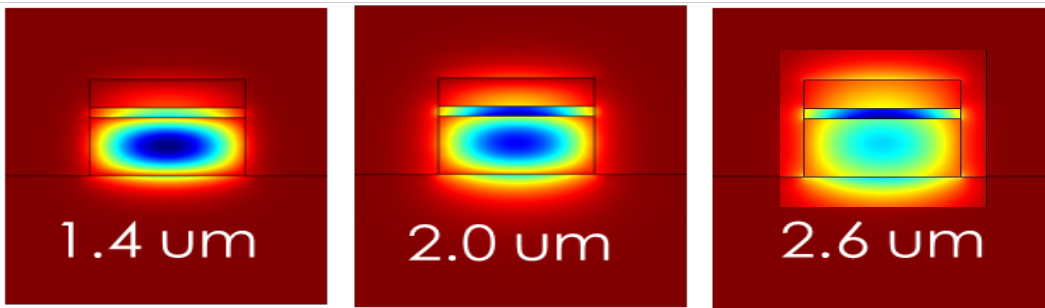
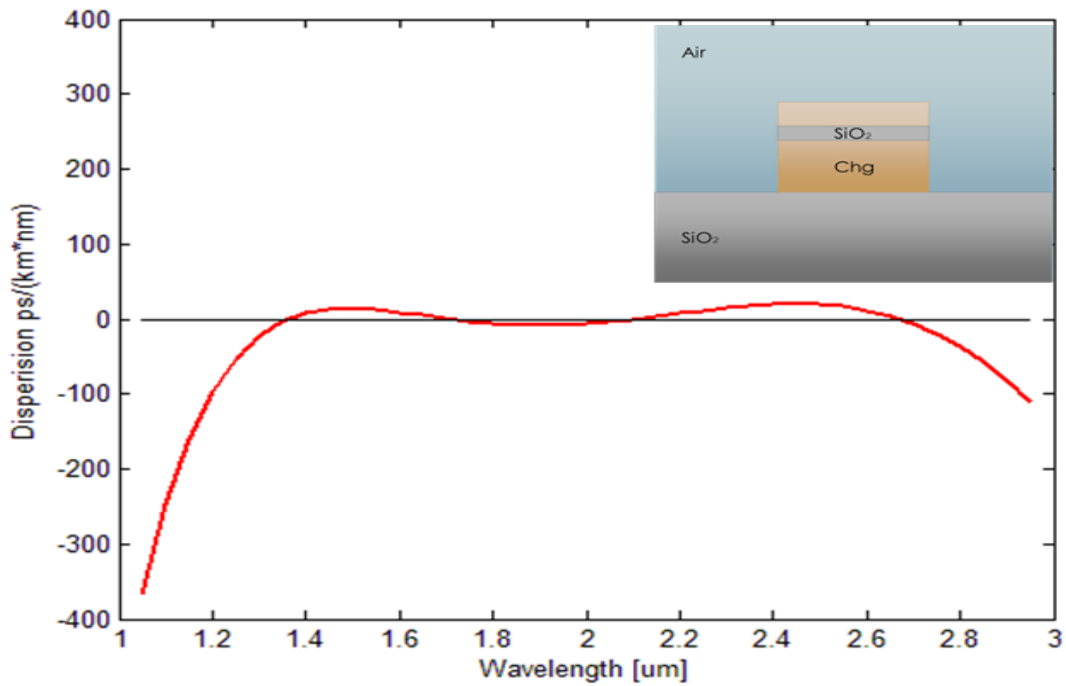


Figure 7: TE dispersion for chalcogenide waveguide with a SiO<sub>2</sub> slot, 1.5  $\mu\text{m}$  width, 1.225  $\mu\text{m}$  total height with a 125 nm slot at 760 height.

An alternative is to only modify the waveguide dimensions to obtain the most appropriate dispersion. Desired transverse-electric (TE) and transverse-magnetic (TM) anomalous dispersion were obtained with channel waveguides 900-nm tall and 2800-nm wide, as shown in Figure 8.

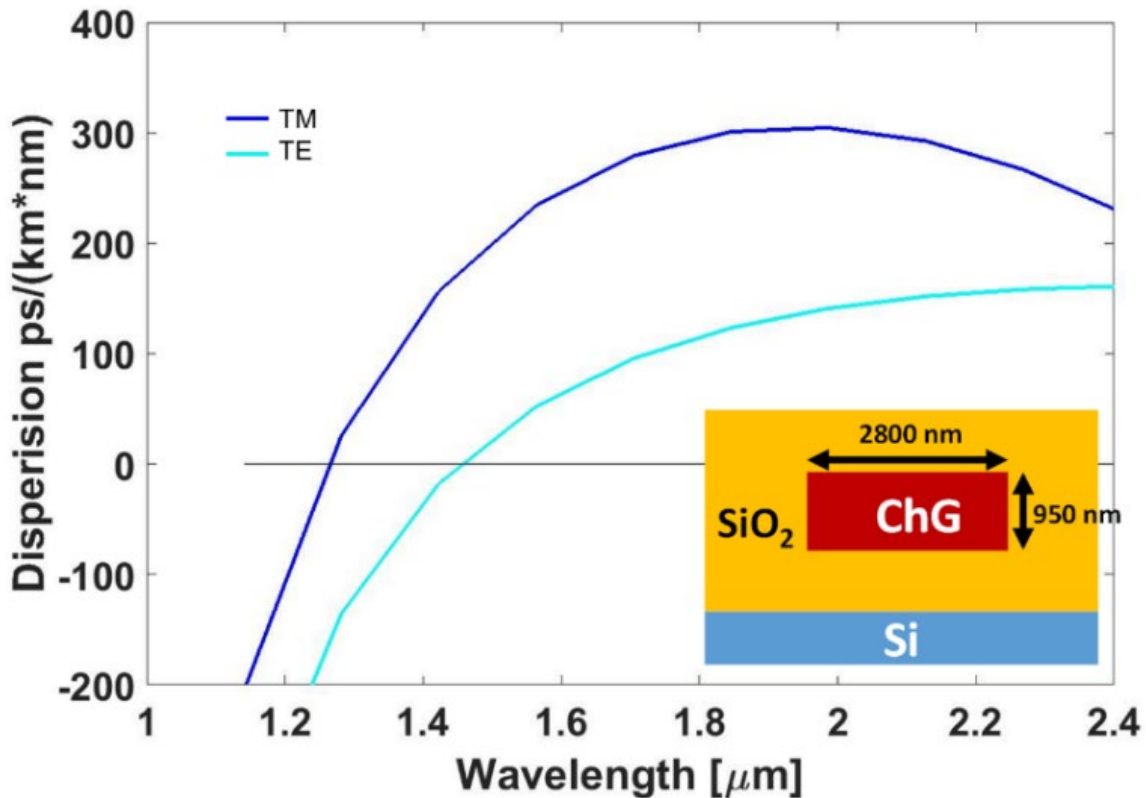


Figure 8: TE and TM dispersion lines for chalcogenide waveguide of 2.8 μm width and 0.95 μm height embedded in silicon dioxide.

### 2.4.2 Fabrication

Some special considerations have to be taken when working with ChG, given that it is a soft material with a very different thermal expansion coefficient, compared to other common materials. After ChG deposition, it is important to add an extra thin film of oxide, only around 10 nm. This measure helps to prevent adhesion of ChG with photoresist, and protects it during development process. We used conventional UV photolithography for the fabrication of 4 cm long waveguides, followed by a chlorine argon dry etch and a

PECVD SiO<sub>2</sub> deposition for passivation. PECVD passivation was done in steps of 250nm deposition each, which helps releasing stress caused during this deposition, and preventing passivation layer to peel off. After fabrication, the sample was diced from the back and carefully cleaved for butt coupling, if this process goes clean, further polishing can be avoided.

### **2.4.3 Measurements and results**

A femtosecond mode-lock laser was used to study the performance of the waveguides. This laser emits pulses centered in 1550 nm, of 500 fs duration and a repetition rate of 90 MHz. With an average power of 160 mW, we get a peak power of ~ 3.5 kW. With an insertion loss of 24 dB, we got over an octave span of supercontinuum generation for TE polarization.

Over an octave span of supercontinuum generation was demonstrated at telecom wavelengths in a Ge<sub>23</sub>Sb<sub>7</sub>S<sub>70</sub> chalcogenide waveguide. We engineered the waveguides dispersion to be anomalous at the pump central wavelength of ~ 1.55 μm for both TE and TM polarizations. In Figure 4, the orange plot correspond to the measurement of a short wavelength optical spectrum analyzer (OSA), whereas the blue to a long wavelength OSA, where the anomalous dispersions and the low-loss highly nonlinear waveguides allow

efficient coherent SC to be achieved, generating a SC that extends from  $\sim 895$  to above 2400 nm.

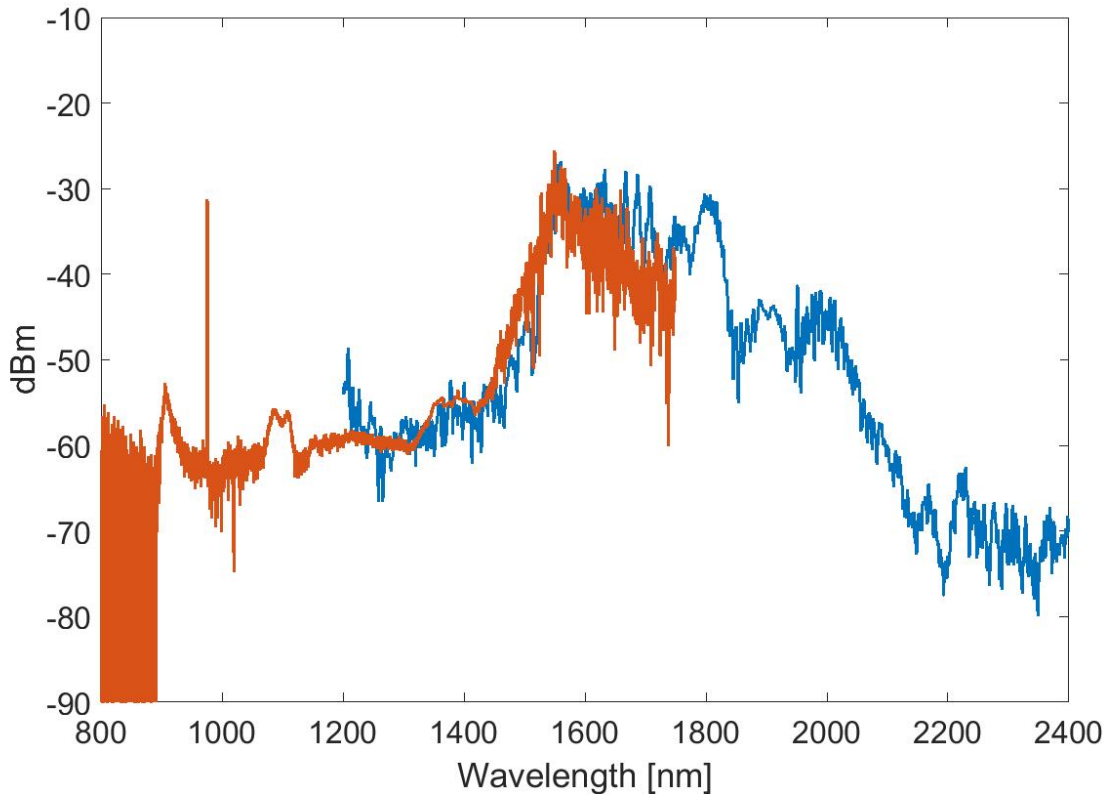


Figure 9: SC spectrum measures for the  $2.8 \times 0.95 \mu\text{m}^2$  chalcogenide waveguide. The orange plot correspond to the measurement of a short wavelength OSA, whereas the blue to a long wavelength OSA.

## 2.5 2D Coupling tapers

The insertion loss of our chips using butt-coupling, is usually around 10 dB per facet. So in order to reduce this number, we worked on the design of non-inverted tapers that would go on top of the waveguide, increasing the cross-sectional area and thus increasing the butt coupling efficiency. As the waveguides are tapered down, the mode is

adiabatically pushed down into the waveguide of interest [36]. A precise refractive index was necessary to achieve this effect, and to overcome this, we built a silicon-rich silicon nitride stack which had the effective refractive index we needed.

Figure 5 shows the mode simulations for various cross-sections along the taper, demonstrating how the mode is pushed down systematically through propagation. It also shows the stack composition and the mode overlap between the tapered fiber and the start point of the non-inverted taper coupler for TM polarization.

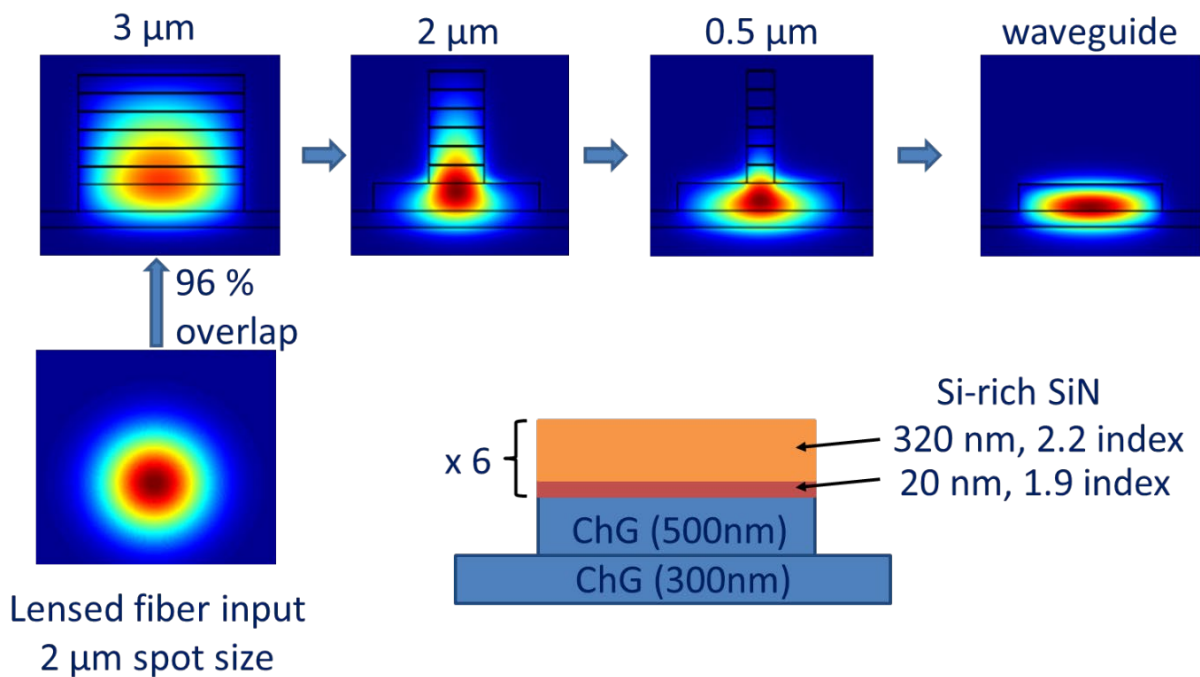


Figure 10: Mode simulations for different cross sections along non inverted taper on chalcogenide ridge waveguides, overlap is shown for butt coupled light coming from a tapered fiber and the structure composition is shown in the lower right corner.

To calculate the overlap efficiency, an input mode profile was created on matlab and swept in height, horizontally aligned to the non-inverted coupler input, and computing the overlap integral at every position until finding the maximum overlap efficiency.

$$A_{eff} = \frac{|\iint_{-\infty}^{\infty} E_f(x, y) * E_w(x, y) dx dy|^2}{\iint_{-\infty}^{\infty} |E_f(x, y)|^2 |E_w(x, y)|^2 dx dy} \quad (3)$$

To proof visually the overlap, the 3D figures shown in were plotted, using the highest overlap positions.

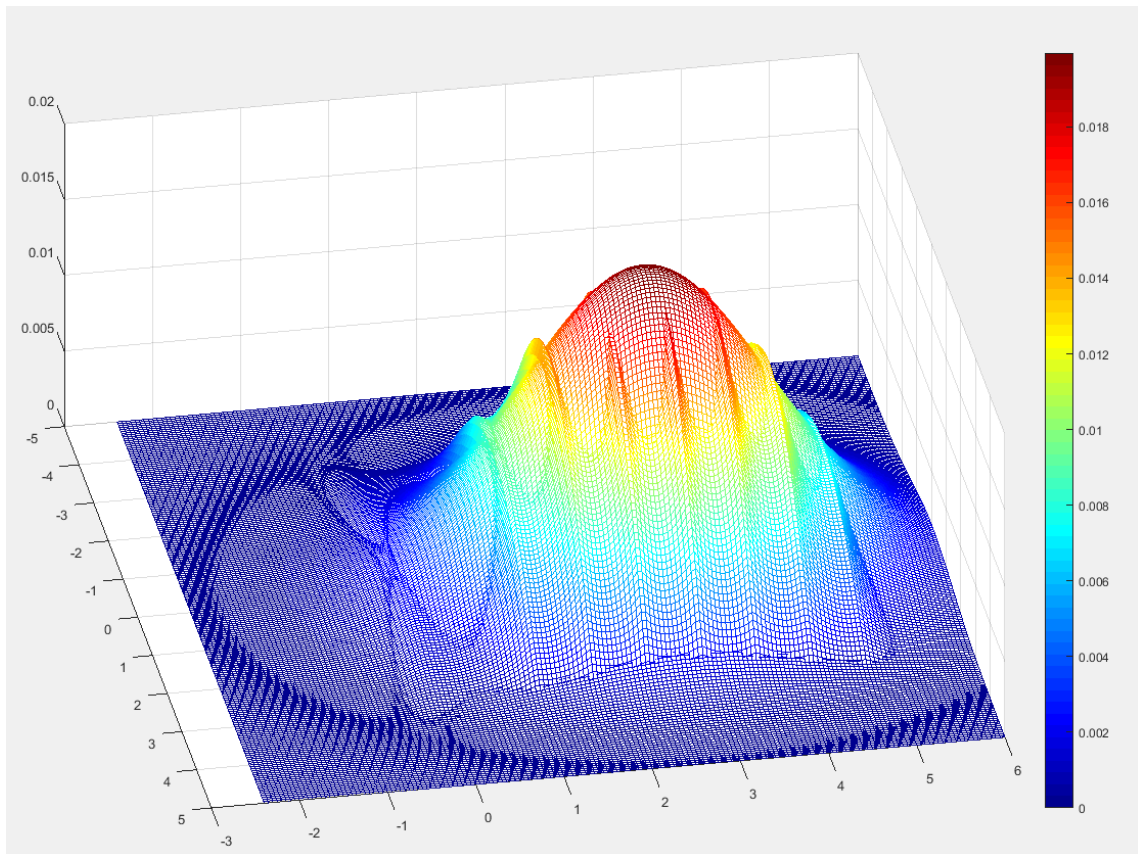


Figure 11: 3D Visual representation of the overlap between the optical mode coming from the fiber and the 2D taper input area.

The measured insertion loss of the chips is 13 dB, which is considerably lower than the more than 20 dB loss for the devices without tapers. And finally supercontinuum was measured for these waveguides, spanning an octave from 1000 nm to 2000 nm (Figure 12).

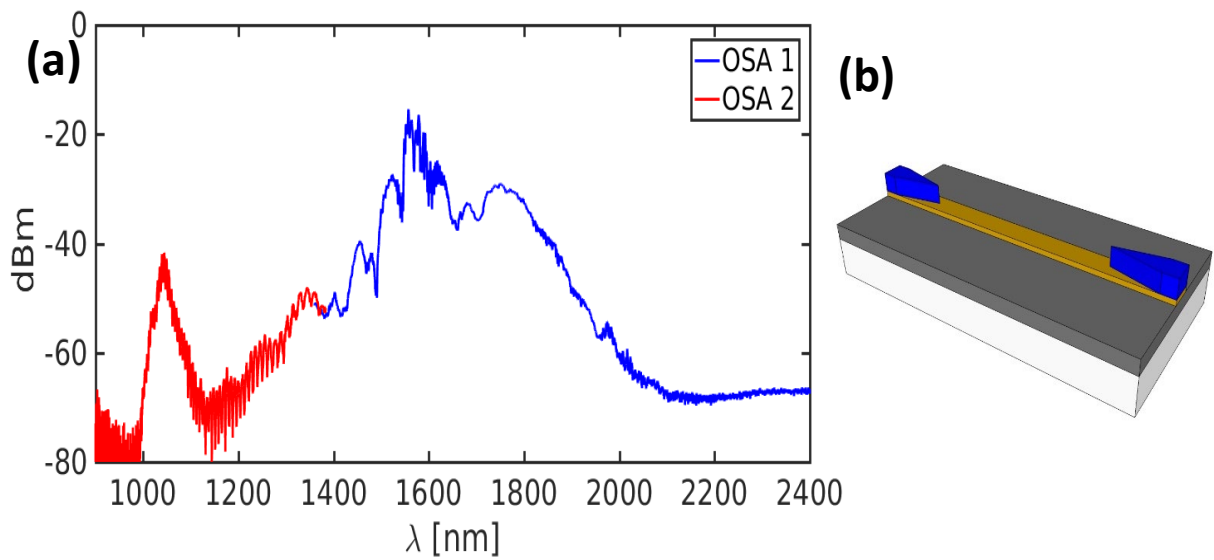


Figure 12: (a) Measured supercontinuum in ChG waveguides with non-inverted 2D tapers. (b) 3D schematic of the actual device.

## **CHAPTER 3: SECOND-HARMONIC GENERATION IN LITHIUM NIOBATE WAVEGUIDES**

### **3.1 Introduction**

Second-harmonic generation (SHG) is a three-waves parametric process, where two photons of the same energy are converted to one with double the energy, or half the wavelength. This happens only in nonlinear media with non-centrosymmetric potential, given by a material lacking inversion symmetry. Lithium niobate is a common choice for second harmonic generation not only because it has a high second order nonlinearity, but because it is an electro-optic material with ferroelectric properties. It is suitable for active optics such as modulators, and it is an excellent option for efficient frequency conversion given that it can be periodically poled to fulfill phase matching condition between the interacting fields.

In this chapter, we are going to briefly discuss two different approaches to tune phase matching condition to a desired waveguide in rib-loaded thin-film LN waveguides.

### **3.2 Phase matching in second-order nonlinear media**

Second-order nonlinear optical effects, arise from perturbations in molecular dipoles, caused by the propagation of an optical field through non-centrosymmetric

media. Therefore, they can be analytically studied by solving the electric field wave equation, using polarization small perturbations. That is:

$$\nabla^2 E - \frac{1}{c^2} \frac{\partial E^2}{\partial t^2} = \mu_0 \frac{\partial^2 (P + P_{NL})}{\partial t^2} \quad (4)$$

With  $E$  the electric field amplitude,  $c$  the speed of light,  $\mu_0$  the vacuum permeability,  $P$  the polarization and  $P_{NL}$  the nonlinear small perturbation that can refer to any second-order nonlinear process. These nonlinear processes are also known as three wave mixing, which implies effects such as SHG ( $\omega + \omega = 2\omega$ ), optical rectification ( $\omega - \omega = 0$ ) sum frequency generation ( $\omega_1 + \omega_2 = \omega_{1+2}$ ) and difference frequency generation ( $\omega_1 - \omega_2 = \omega_{1-2}$ ). Equation (4) is simplified by applying the slowly varying envelope approximation and unidimensional propagation, leading us to:

$$\frac{\partial \mathcal{E}}{\partial z} + \frac{\alpha}{2} \mathcal{E} = i \frac{\omega}{2nc\epsilon_0} \wp_{NL} e^{i(k_{NL}-k)z} \quad (5)$$

Where  $\mathcal{E}$  and  $\wp_{NL}$  are the amplitudes of the electric and nonlinear polarization fields respectively,  $\alpha$  is the linear loss,  $\epsilon_0$  is the vacuum permittivity and  $k_{NL} - k$  is the difference between nonlinear and linear wave-vectors. For instance we ignore linear losses, supposing that we are far from resonance, and focus in second-harmonic generation, where we have one equations at the base frequency and another at the doubled frequency.

$$\frac{\partial \mathcal{E}(\omega)}{\partial z} = i \frac{\omega}{2n_\omega c \epsilon_0} \wp_{NL}(\omega) e^{i(k_{NL}-k)z} \quad (6)$$

and

$$\frac{\partial \mathcal{E}(2\omega)}{\partial z} = i \frac{\omega}{2n_{2\omega}c\epsilon_0} \wp_{NL}(2\omega) e^{i(k_{NL}-k)z} \quad (7)$$

With  $\wp_{NL}(\omega) = 2 \frac{\epsilon_0}{2} \chi^{(2)} \mathcal{E}^*(\omega) \mathcal{E}(2\omega)$  and  $\wp_{NL}(2\omega) = \frac{\epsilon_0}{2} \chi^{(2)} \mathcal{E}(\omega) \mathcal{E}(\omega)$ , we get to the coupled wave equations (8) and (11), which describe the interaction of the fundamental and second-harmonic fields through propagation:

$$\frac{\partial \mathcal{E}(\omega)}{\partial z} = i \frac{\omega}{n_{\omega}c} d_{eff} \mathcal{E}^*(\omega) \mathcal{E}(2\omega) e^{-i(2k_{\omega}-k_{2\omega})z} \quad (8)$$

$$\frac{\partial \mathcal{E}(2\omega)}{\partial z} = i \frac{\omega}{n_{2\omega}c} d_{eff} \mathcal{E}(\omega) \mathcal{E}(\omega) e^{i(2k_{\omega}-k_{2\omega})z} \quad (9)$$

where  $d_{eff}$  is half the second order susceptibility.

Considering weak SHG, which means negligible fundamental signal depletion ( $\mathcal{E}(\omega, z = 0) \cong \mathcal{E}(\omega, z = L)$ ), and only fundamental input signal ( $\mathcal{E}(2\omega, z = 0) = 0$ ), we can solve equation (11) for SHG signal through propagation.

$$\mathcal{E}(2\omega, z = L) = i \frac{\omega}{n_{2\omega}c} d_{eff} \mathcal{E}(\omega) \mathcal{E}(\omega) e^{\frac{i(2k_{\omega}-k_{2\omega})L}{2}} \text{sinc} \left( \frac{(2k_{\omega} - k_{2\omega})L}{2} \right) L \quad (10)$$

which squared is proportional to the intensity:

$$I(2\omega, z = L) = \left| \frac{\omega d_{eff}}{n_{2\omega}c} \mathcal{E}^2(\omega) \right|^2 \text{sinc}^2 \left( \frac{(2k_{\omega} - k_{2\omega})L}{2} \right) L^2 \quad (11)$$

As it can be seen from equation (11), the SHG signal evolves as a *sinc* function, which means that is maximum when its argument is equal to zero. This condition happens when wave-vector's difference is zero, this is the so called "phase-matching condition". This

equation shows us that the conversion efficiency oscillates through propagation, as depicted in Figure 13. Given that perfect phase matching condition is not realistic, we need to use alternative methods to maximize our conversion efficiency. This is where periodically poling comes into play.

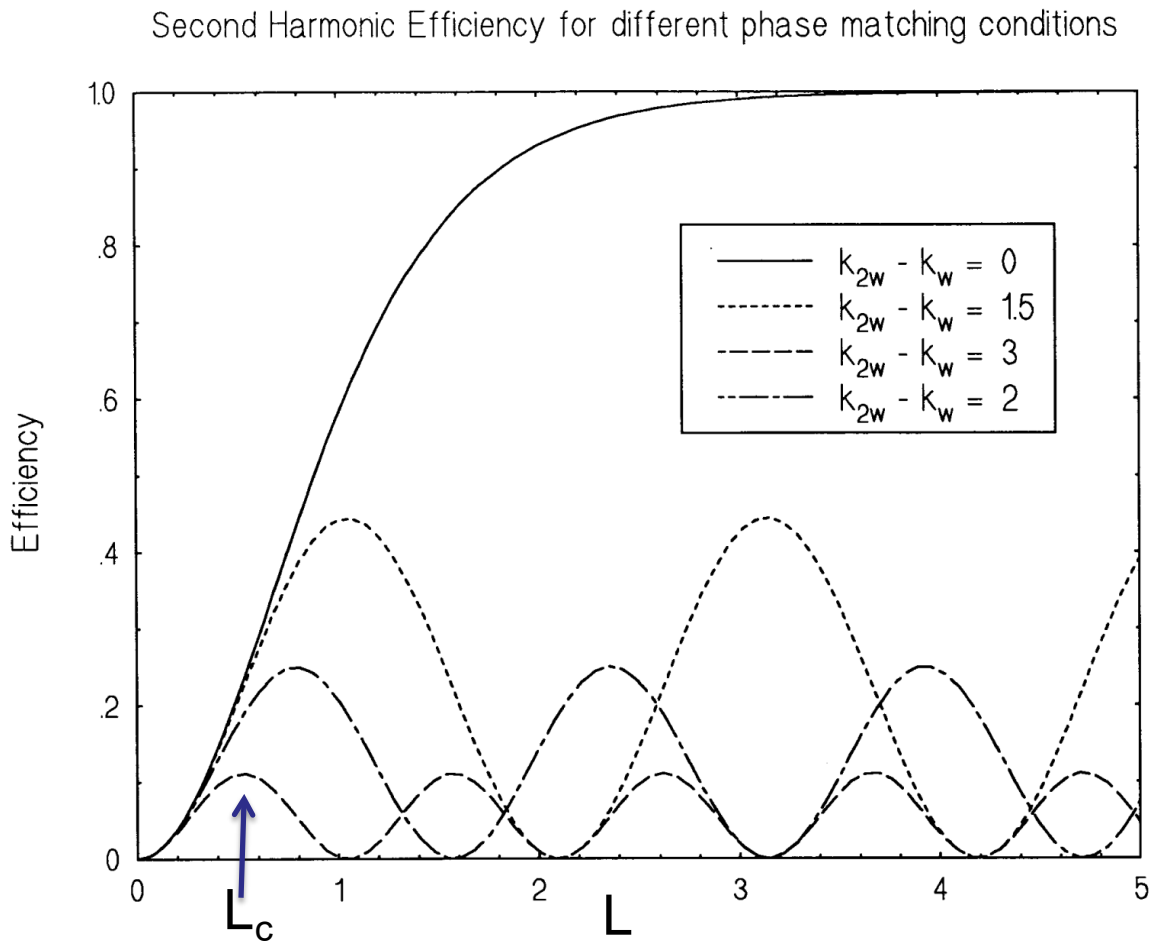


Figure 13: a) SHG efficiency through propagation length, for different phase difference conditions. We call it coherence length  $L_c$  to the length where maximum efficiency happens. Image from [37].

Lithium niobate is not only a second-order nonlinear material, but it is also a ferroelectric, which allows us to permanently change the molecules dipolar orientation with the application of an external electric field. We can picture from Figure 13, that if we shift these dipoles at the length where conversion efficiency is maximum, known as coherence length  $L_c$ , the light will encounter the material shifted in phase, instead of continue to monotonous propagation. This can lead to continuous rise of the conversion efficiency if the material dipoles are shifted in periodic domains, which means, periodically polling the material. To choose the proper periodicity for the conversion, it is necessary to calculate the value of  $L_c$ , using  $L_c = \pi/\Delta k$ . A more detailed study of this nonlinearity can be found in [37].

### **3.3 Thin film periodically poled lithium niobate**

Second-order optical nonlinear effects (second-harmonic and sum-frequency generation) were demonstrated in the telecommunication band by periodic poling of thin films of lithium niobate wafer-bonded on silicon substrates and rib-loaded with silicon nitride channels to attain ridge waveguide with cross-sections of  $\sim 2 \mu\text{m}^2$ . A nonlinear conversion of 8% is obtained with a pulsed input in 4 mm long waveguides. The choice of silicon substrate makes the platform potentially compatible with silicon photonics, and therefore may pave the path towards on-chip nonlinear and quantum-optic applications. The fabricated device is shown in Figure 6a, and Figure 6b shows one of the measurements

performed using the same mode lock laser I used for supercontinuum experiments. The ultimate proof for successful poling is demonstration of nonlinear optical processes that require QPM. The fabricated 4-mm long thin film PPLN waveguides were optically characterized by coupling light in and out of the chips by lensed fibers. The propagation losses at the pump and second harmonic wavelength are  $< 1$  dB/cm, obtained by analyzing the insertion loss across a number of waveguides. The material absorption of the SiN rib material is  $< 1$  dB/cm and  $< 0.2$  dB/cm at the fundamental and second harmonic wavelength respectively, measured on a Metricon prism-coupling system. The coupling loss measured per facet at the pump wavelength is  $\sim 10$  dB. The coupling loss at the second harmonic wavelength is marginally higher due to the multimode nature of the lensed fibers used. The coupling losses can be potentially reduced by the use of appropriately-designed input and output waveguide tapers, or the use of free-space lensed input and output coupling.

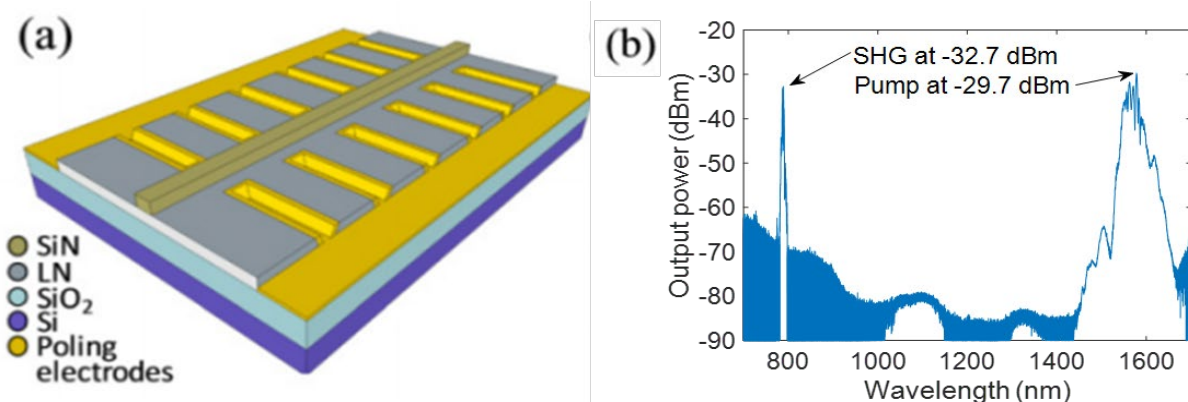


Figure 14: a) Periodically poled lithium niobate waveguide example, period can be designed to fulfill phase match condition of the required wavelength. b) Clear second harmonic signal at around 788 nm detected by an optical spectral analyzer. Results published in [26].

These devices are 4 mm long and the cross-sections are significantly smaller than traditional PPLN wavelength converters. The compact size along with the use of a silicon substrate demonstrates the compatibility of efficient  $\chi^{(2)}$ -based nonlinear photonic devices with silicon photonics for potential on-chip nonlinear and quantum-optic applications.

To prove that the phase matched wavelength can be freely selected by the poling period, we did the same experiment for a 1950 nm source. The measured SHG spectrum is depicted in Figure 15.

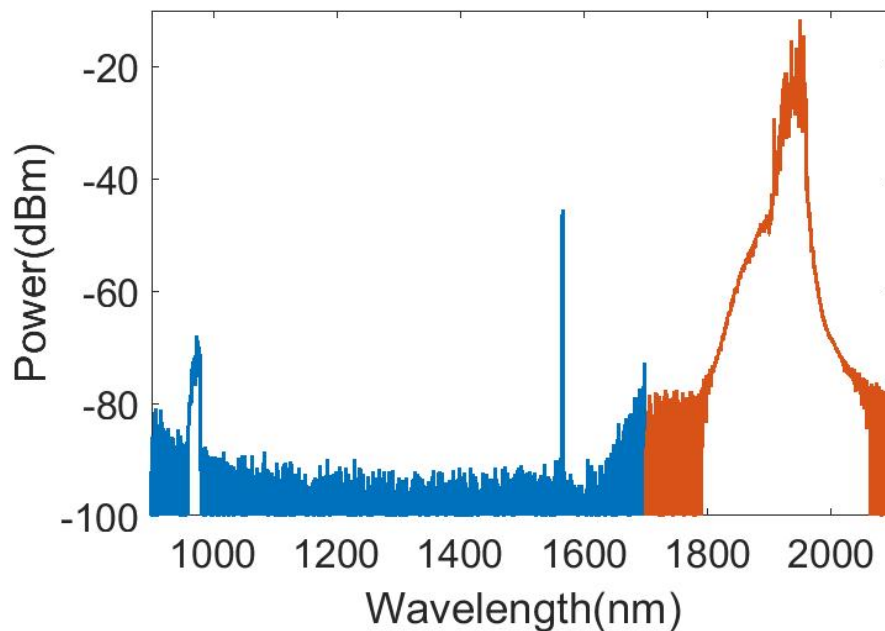


Figure 15: SHG for a 1950 nm pump, using a periodically poled lithium niobate waveguide, generating a converted signal at 973.2 nm. Results published in [38].

### **3.4 Mode-shape modulation on thin film lithium niobate**

An alternative to periodic polling, consists in adding a periodic structure to the rib waveguide on top of lithium niobate. This effect is known as grating-assisted quasi-phase matching, which we implemented in our experiments, by added periodicity to a loaded rib waveguide on lithium niobate as shown in Figure 7(a).

We characterized our 4.9-mm-long waveguides using a pulsed source at a 100 MHz repetition rate with a 500 fs pulse duration. The spectrum is centered at 1560 nm, with an average power of 84 mW. The pump light was coupled on and off the chip through lensed fibers, with an estimated coupling loss of 6.5 dB/facet. A fiber-based polarization controller was used at the input to align the polarization in the horizontal direction, corresponding to the Z-axis of the LN film and the TE mode of the waveguide. The output light from the waveguide was directed to an optical spectrum analyzer. The obtained spectrum trace in Figure 7(b), shows the generated SH signal at 784 nm with a peak power spectral density of  $-33.3$  dBm/nm for the signal. The pump shows a power spectral density of  $-16$  dBm/nm at the corresponding phase-matched wavelength of 1568 nm, indicating a reduction of  $-17.3$  dB from the SHG process.

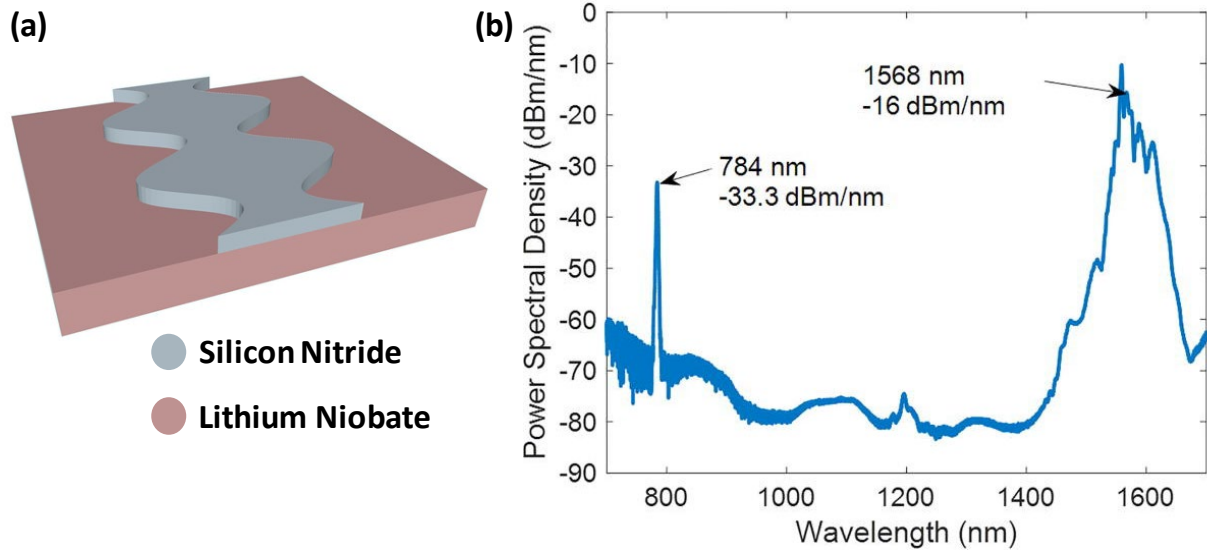


Figure 16: a) Mode-shape modulated rib on lithium niobate waveguide, period can be designed to fulfill phase match condition of the required wavelength. b) Second harmonic signal at around 784 nm detected by an optical spectral analyzer. Results published in reference [25].

Mode-shape modulation is employed to obtain poling-free quasi-phase matching in thin-film lithium niobate. Second harmonic generation is demonstrated at a signal wavelength of 784 nm, utilizing near-infrared pulsed pumping. This implementation is directly applicable to other conventional second-order nonlinear integrated waveguide platforms that are not able to be electrically poled.

## **CHAPTER 4: HYBRID INTEGRATION OF CHALCOGENIDE AND LITHIUM NIOBATE WAVEGUIDES**

*Partial contents of this chapter have been published in IEEE Photonics Journal. 2018 as: Amirmahdi Honardoost, Guillermo Fernando Camacho Gonzalez, Saeed Khan, Marcin Malinowski, Ashutosh Rao, Jean-Etienne Tremblay, Anupama Yadav, Kathleen Richardson, Ming C Wu, Sasan Fathpour, "Cascaded integration of optical waveguides with third-order nonlinearity with lithium niobate waveguides on silicon substrates," IEEE Photonics Journal 10, no. 3, 1-9 (2018).*

*Partial contents of this chapter have been published in OSA Applied Optics, 2019 as: Guillermo Fernando Camacho Gonzalez, Marcin Malinowski, Amirmahdi Honardoost, and Sasan Fathpour, "Design of a hybrid chalcogenide-glass on lithium-niobate waveguide structure for high-performance cascaded third- and second-order optical nonlinearities," Appl. Opt. 58, D1-D6 (2019).*

### **4.1 Introduction**

As mentioned before, several shortcomings are well known for silicon photonics when it comes to nonlinear optical applications. Silicon (Si) inherently lacks the second-order optical susceptibility ( $\chi(2)$ ) due to its centrosymmetric lattice structure. This restricts convenient utilization of Si for applications like second-harmonic generation (SHG).

Additional to this fundamental issue, is the presences of two-photon and free-carrier absorptions (TPA and FCA) at the required high optical intensities which limits the exploitation of the large third-order optical susceptibility ( $\chi(3)$ ) of Si [5, 12, 39, 40]. Moreover, all-silicon optical modulators which operate based on free-carrier plasma dispersion effect, while having demonstrated high data transmission rates, suffer from low extinction ratios [24]. Heterogeneous integration of materials with better optical nonlinearities and electro-optical properties on Si substrates have been more recently explored as a solution to the aforementioned problems [12]. It is also highly desired to integrate the  $\chi(2)$  and  $\chi(3)$  nonlinearities on the same chip for some applications such as optical frequency comb generation based on coherent supercontinuum generation (SCG) stabilized by f-to-2f carrier-envelope offset (CEO) locking [41, 42].

Lithium niobate ( $\text{LiNbO}_3$ , LN), for instance is one of the heavily investigated materials for nonlinear optical applications. Transparency in a broad range of the electromagnetic spectrum (0.4-5  $\mu\text{m}$ ), and possessing strong second-order nonlinearity, as well as large electro-optic coefficient [12] make LN an ideal material of choice for integration with Si photonics for applications such as SHG [23, 25, 26], and optical modulation [27, 24, 21], as well as generation of entangled photon pairs in quantum optics [43, 44]. Conventional LN devices which are fabricated based on dopant diffusion [45] or proton-exchange processes [46] are bulky in general and exhibit low efficiency in terms of power consumption and device footprint hence hampering the desired large-scale integration

capability. Compact LN waveguides based on bonding of thin films of LN on oxidized Si substrate have been demonstrated and pursued towards satisfying the requirement of large-scale integration. Moreover, by rib loading the LN with refractive index-matched materials such as tantalum pentoxide ( $\text{Ta}_2\text{O}_5$ ) or silicon nitride ( $\text{Si}_3\text{N}_4$ ), high optical confinement has been achieved in LN cross-section of these submicron hybrid waveguides which is essential for nonlinear applications [21, 27].  $\text{Si}_3\text{N}_4$  and chalcogenide glass (ChG), due to their negligible TPA coefficient, are also among commonly employed materials fabricated on oxidized Si for  $\chi^{(3)}$ -based nonlinear applications such as four-wave mixing (FWM) [12].

Recently, heterogeneous integration of  $\text{Si}_3\text{N}_4$  waveguides with thin-film LN on Si has been demonstrated towards the  $\chi^{(2)}$  and  $\chi^{(3)}$  integration goal [47]. As discussed earlier,  $\chi^{(3)}$ -based nonlinearity utilization of ChG glass outperforms that of Si due to the absence of FCA and negligible effect of TPA in ChG. Moreover, nonlinear refractive index of ChG ( $\sim 100 \times 10^{-20} \text{ m}^2/\text{W}$ ) is almost 4 times larger than that of  $\text{Si}_3\text{N}_4$  ( $26 \times 10^{-20} \text{ m}^2/\text{W}$ ) [4]. These properties combined with the possibility of obtaining high optical confinement and low-loss waveguides make ChG another attractive candidate to be exploited for various nonlinear applications [48, 49, 31, 50].

## 4.2 Integrability demonstration

The work presented in this letter reports on a heterogeneous platform for integrating ChG glass waveguides and thin-film LN on the same Si chip. Carefully designed mode-converting tapers are employed for adiabatic optical mode transition from ChG to hybrid LN waveguides and vice versa. In comparison to the previous report on integration of  $\text{Si}_3\text{N}_4$  waveguides with thin-film LN [44], our proposed platform has the advantages of eliminating the need for LN bonding at the final stages of the processing, and offers a simpler and more straightforward fabrication process.

### 4.2.1 Simulations

The schematic of the integrated platform is shown in Figure 8. The optical mode profiles of the structure are simulated by using Lumerical™ Mode Solutions. The fundamental transverse-electric (TE) mode at 1550 nm is shown at different cross-sections of the structure. The mode at the input is mainly distributed in the ChG rib due to its higher refractive index compared to  $\text{Si}_3\text{N}_4$ . By introducing the shown tapered region, the optical mode gradually transfers into the  $\text{Si}_3\text{N}_4$ -LN lower waveguide, where 50% of the mode distribution is confined within the LN thin film. The top-left inset depicts the optical mode transition from the upper waveguide region (ChG) to the lower one ( $\text{Si}_3\text{N}_4$ -LN) and vice versa.

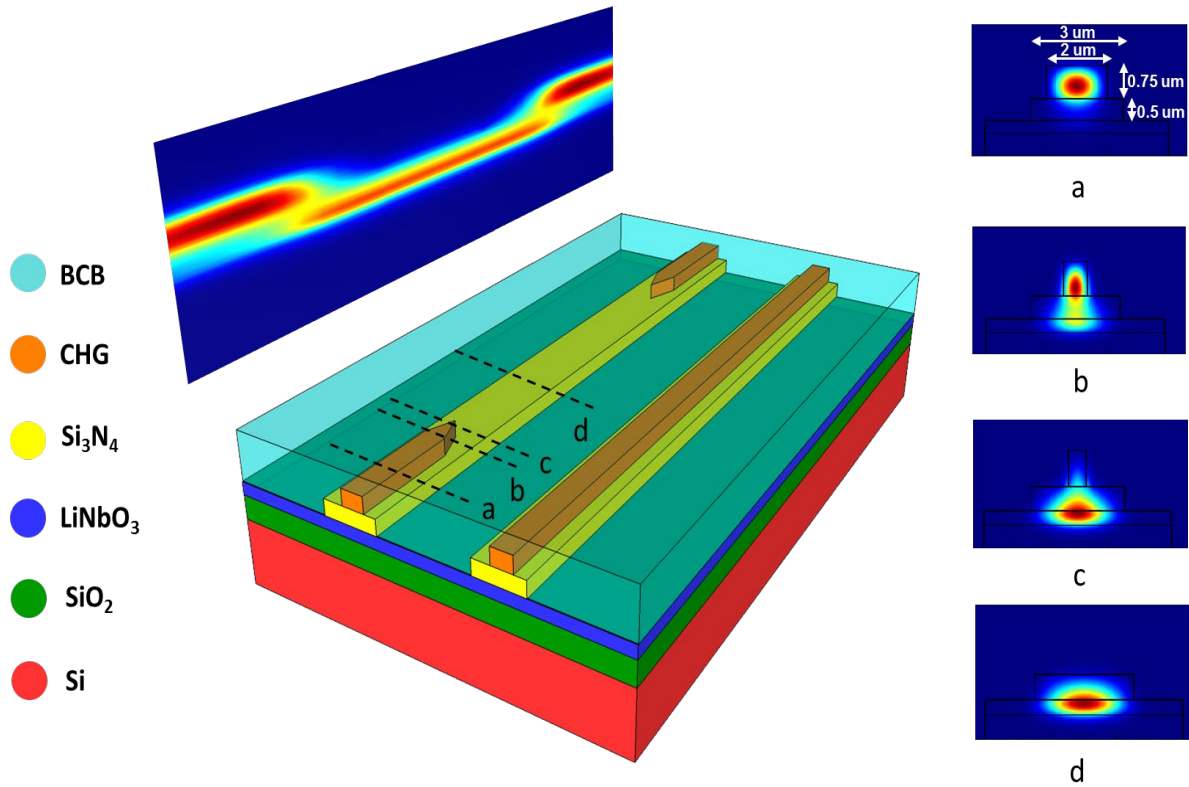


Figure 17: Schematic of the integrated ChG-LN as well as the reference waveguides. Optical mode profiles of the structure are also shown for fundamental TE input at 1550 nm for different cross-sections. Adiabatic mode transition is shown in the inset.

Adiabatic mode transition for negligible coupling loss is found to be occurring at taper's length of  $> 100 \mu\text{m}$  according to Lumerical™ simulations as depicted in Figure 9a. The inset in Figure 8 shows the adiabatic TE mode transition for  $500 \mu\text{m}$  length of the taper. Meanwhile, coupling efficiency for TM input mode is 90% according to simulations.

Figure 9b shows the simulated coupling efficiency of the tapers versus the wavelength which suggests a large bandwidth for the proposed structure. In addition to the large optical bandwidth, high error tolerance is also predicted by the simulation results. Figure 9c depicts the coupling efficiency of the taper versus the width of its tip. Coupling

efficiency is also shown versus the misalignment between the centers of the ChG waveguide/taper and Si<sub>3</sub>N<sub>4</sub>-LN waveguide in Figure 9d.

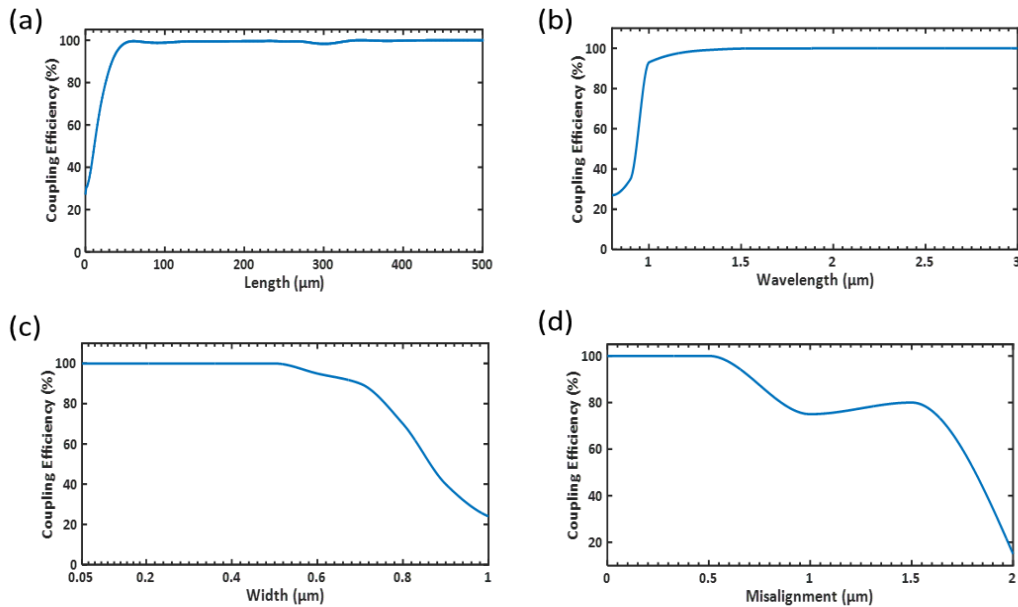


Figure 18: Coupling efficiency of the mode-converting tapers vs. (a) Length of the taper, (b) Different wavelengths, (c) The width of the taper’s tip, and (d) Misalignment between the centers of the ChG waveguide/taper and Si<sub>3</sub>N<sub>4</sub>-LN waveguide.

## 4.2.2 Fabrication

The fabrication process begins with a 300-nm-thick X-cut LN thin film on a 2-μm-thick layer of buried SiO<sub>2</sub> on Si Substrate. A 500-nm-thick layer of Si<sub>3</sub>N<sub>4</sub> is deposited on the LN thin films using plasma-enhanced chemical vapor deposition (PECVD) and patterned using ZEP 520-A resist and electron-beam lithography (EBL) by a Leica EBPG5000 + writer followed by dry etching using inductively-coupled plasma reactive-ion etching (ICP-RIE)

to form the 3- $\mu\text{m}$ -wide ribs. Then the 750-nm-tall by 2- $\mu\text{m}$ -wide strips of thermally-evaporated ChG glass,  $\text{Ge}_{23}\text{Sb}_7\text{S}_{70}$ , is deposited on top of  $\text{Si}_3\text{N}_4$  ribs and patterned similarly to form the ChG waveguides, as well as the mode-converting tapers. 10-mm long reference waveguides without tapers are also fabricated on the same chip (as shown in Figure 7) which are used for measuring the mode transition loss introduced by the tapers. Finally, a 2  $\mu\text{m}$  layer of benzocyclobutene (BCB) is spun and cured on top to serve as the top cladding layer for the devices.

### **4.2.3 Measurements and results**

The devices are characterized by using a tunable single-mode continuous-wave (CW) laser source (Keysight 8164B) with spectral range of 1490-1630 nm. Then, the TE output from a polarization controller is end-butted coupled into the waveguides through a lensed fiber. Another lensed fiber couples the light out of the waveguides into a photodetector (Newport 1931-C) in order to measure the output optical power and hence the insertion loss. Both the ChG- $\text{Si}_3\text{N}_4$ -LN integrated devices as well as the reference waveguides (with no tapers) are characterized. The measurements are also done for TM input polarization for the total operating wavelength range of the CW laser source. The results are presented in Figure 10.

Figure 10(a) shows the output power difference between the integrated and reference waveguides for TE and TM polarization for the 1550 nm wavelength range. Results from Figure 10(b) confirm that for TE polarization, there is only  $\sim 3$  dB power difference between the integrated and reference waveguides from 1550 to 1560 nm, i.e.,  $\sim 1.5$  dB loss per mode-converting tapers for 1550 nm wavelength range. As depicted in Figure 10(b), the measurements which are performed for the TM polarization input results in average  $\sim 0.5$  dB more loss compared to the TE measurement which is in accordance with the simulation prediction (90% coupling efficiency).

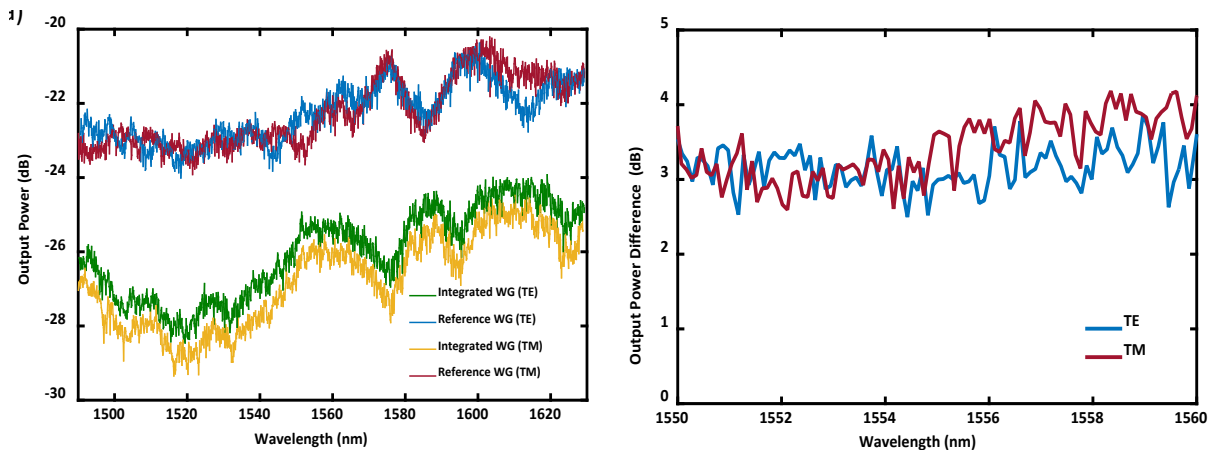


Figure 19: (a) Optical spectrum of output power for integrated as well as the reference waveguides for both TE and TM input polarization for 1490-1630 nm wavelength range, and (b) Optical spectrum of output power difference integrated and reference waveguides for TE and TM input polarization for 1550-1560 nm wavelength range.

For nonlinear characterization, wavelength conversion via FWM is measured for the integrated as well as the reference waveguides of the chip. The setup for this experiment is depicted in Figure 11. Two tunable single-mode CW laser source (Keysight 8164B and

LUNA Phoenix 1400 with spectral ranges of 1490-1630 nm and 1515-1565 nm respectively) are used for the input. A polarization controller is connected at the output of the LUNA laser in order to make it collinear with the polarization of Keysight laser. Both laser signals are then combined in a 3-dB coupler and amplified using an erbium-doped fiber amplifier with operating wavelength range of 1526-1566 nm. End-butt coupling with tapered fibers is used to couple the combined signals into and out of the waveguides. The tapered fibers minimum spot size is 2  $\mu\text{m}$  FW1/e2M. The output signal is then followed by a 99:1 splitter, where one percent goes to the power meter for monitoring the alignment and ninety-nine percent is received by a Yokogawa AQ6370B OSA with operating wavelength range of 600-1700 nm.

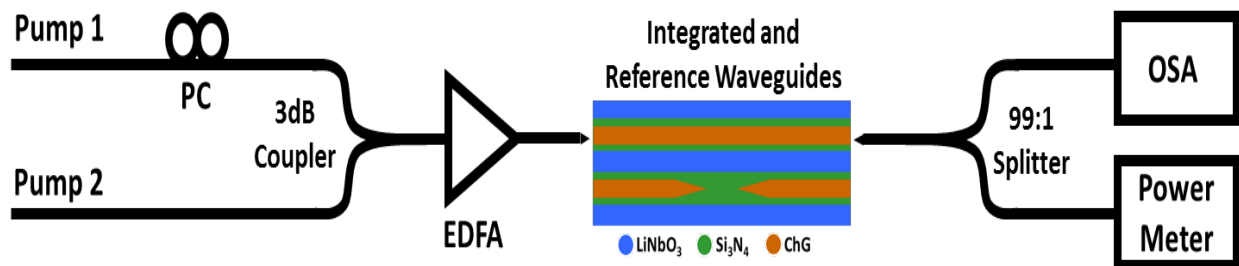


Figure 20: Schematic of the experimental setup for wavelength conversion via FWM. PC: Polarization Controller, EDFA: Erbium-doped fiber amplifier, OSA: Optical spectrum analyzer.

The converted signal we were collecting using the conventional FWM experiment, using 1 pump and 1 idler to get 1 converted signal, was so low that we couldn't detect it in the OSA, to overcome this drawback we amplified both input lasers in a more general FWM experiment. So both input lasers are used as pumps and idlers simultaneously, generating

two FWM converted signals with higher intensity. This nonlinear experiment was performed in both tapered and reference waveguides to confirm both the light coupling into chalcogenide and the capability of the chip to generate third order nonlinearities. The transmitted spectrum through the reference and tapered waveguides for the amplified inputs to 327 mW is shown in Figure 12. The two higher peaks correspond to the tunable lasers output emissions at  $1560.13 \pm 0.01$  and  $1560.99 \pm 0.01$  nm. We choose these wavelengths because they are within a region of relatively constant amplification of the EDFA. And the weak signals at the sides correspond to FWM generation at  $1559.27 \pm 0.01$  in the left and  $1561.86 \pm 0.01$  in the right.

We made a numerical study of the FWM results by solving the nonlinear coupled equations:

$$\frac{dA_k}{dz} = -\frac{\alpha}{2}A_k + i\gamma \left( |A_k|^2 + 2 \sum_{i \neq k}^4 |A_i|^2 \right) A_k + i2\gamma A_l A_m A_n^* e^{\pm i\Delta k_1 z} + i\gamma (A_l)^2 A_m^* e^{i\Delta k_2 z} \quad (12)$$

$$\frac{dA_l}{dz} = -\frac{\alpha}{2}A_l + i\gamma \left( |A_l|^2 + 2 \sum_{i \neq l}^4 |A_i|^2 \right) A_l + i\gamma (A_m)^2 A_n^* e^{\pm i\Delta k_3 z} + i2\gamma [A_k A_n A_m^* e^{\mp i\Delta k_1 z} + A_k A_m A_l^* e^{\mp i\Delta k_2 z}] \quad (13)$$

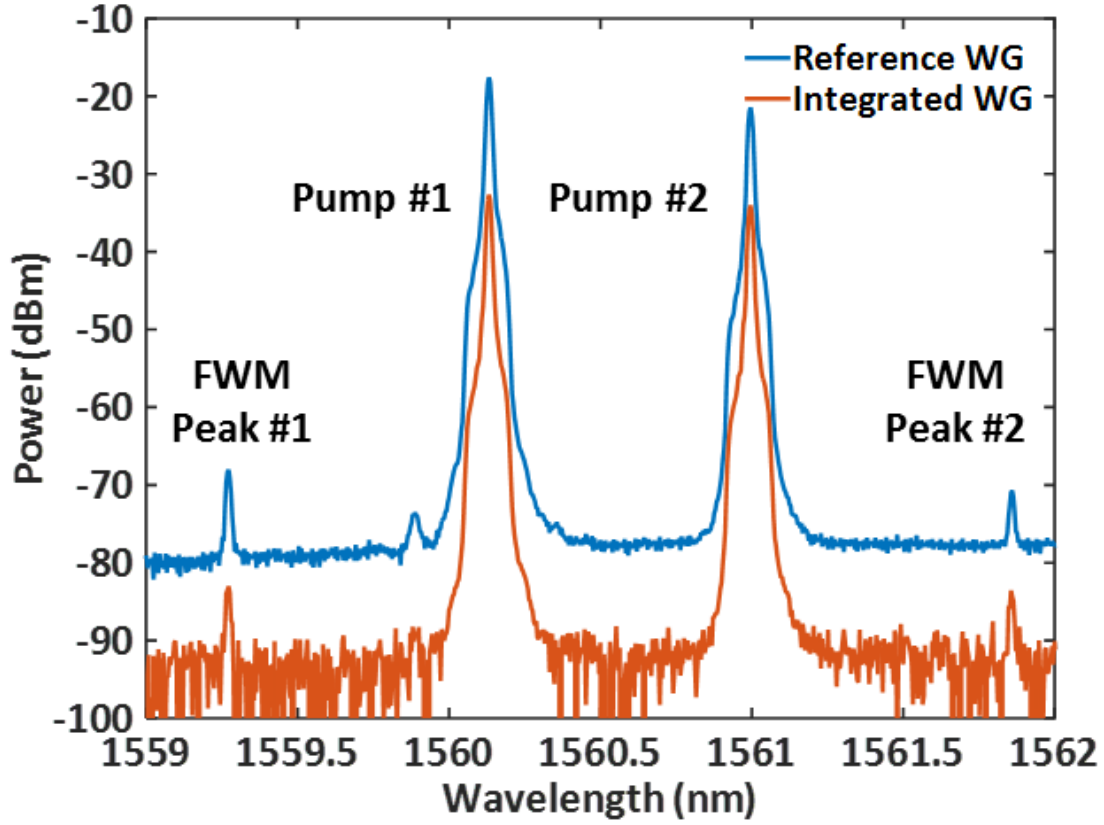


Figure 21: Bit rate-product evolution in time, solid circles represent the emerging of new technologies. Image from [4].

With sub-indices  $k = 1,4$ ,  $l = 2,3$ ,  $m = 3,2$  and  $n = 4,1$ , where  $A_i$  are field amplitudes,  $\alpha$  is the linear propagation loss, and  $\gamma$  the nonlinear parameter  $\gamma = \frac{n_2\omega}{cA_{\text{eff}}}$ . These equations

were obtained by solving  $P^{(3)} = \frac{1}{2}\chi^{(3)}\epsilon_0 EE^*E + c.c.$  for  $E = \sum_{n=1}^4 E_n e^{i(k_n z - \omega t)}$ , and

considering three phase matching conditions:

$$\Delta k_1 = k_2 + k_3 - k_1 - k_4 \quad (14)$$

$$\Delta k_2 = 2k_2 - k_1 - k_3 \quad (15)$$

$$\Delta k_3 = 2k_3 - k_2 - k_4 \quad (16)$$

Corresponding to three possible physical processes, i.e. the exchange of energy between the implicated waves to create a photon of either  $k_1$  or  $k_4$  wave vector.

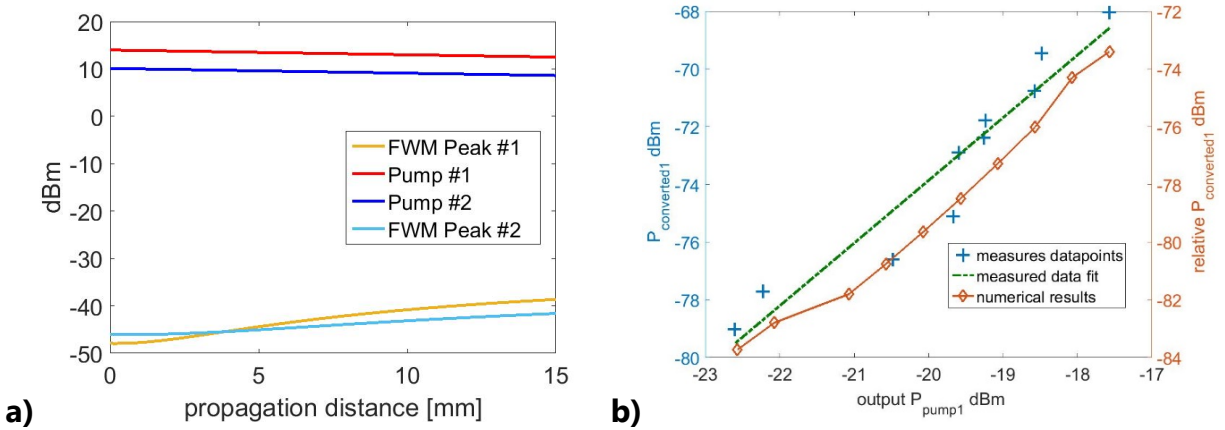


Figure 22: a) Evolution of pumps and converted signals with propagation. b) Comparison between measured and numerically calculated conversion at different input powers.

In Figure 13a, we show the power evolution of the pumps and converted signals in propagation. Here we considered an input of 24 dBm, 11 dB of coupling losses, 1 dB/cm of propagation loss and the nonlinear parameter  $\gamma$  is estimated to be 13 m/W. The wave vectors  $k_i$  were calculated with the help of COMSOL, where we got the effective refractive indices of the implicated wavelengths. We can notice that the converted Peak #1 grows faster than Peak #2, this is in good accordance with the experiment, with a waveguides length of about 10 mm.

Figure 13b shows the measured output converted Peak #1 vs output Pump #1 for different input powers with its linear fit, compared to numerically obtained values.

Numerical results were shifted by considering output coupling losses, so we show relative power for it. We can see the similarity between the fit and the numerical results, which confirm the estimated value of the nonlinear parameter.

In summary, a heterogeneous platform is demonstrated by integrating  $\text{Ge}_{23}\text{Sb}_7\text{S}_{70}$  ChG glass and  $\text{Si}_3\text{N}_4$ -LN waveguides on Si substrate. This platform provides an efficient method of integrating materials with large  $\chi^{(2)}$  and  $\chi^{(3)}$  coefficients on the same chip. Adiabatic optical mode transition from ChG to  $\text{Si}_3\text{N}_4$ -LN is achieved through carefully designed mode-converting tapers with measured  $\sim 1.5$  dB loss for TE and  $\sim 1.75$  dB loss for TM input polarization for 1550 nm wavelength range. Wavelength conversion via FWM is measured for the integrated and the reference waveguides. Further work will continue with the integration of chalcogenide and lithium niobate on the same chip. This time proving both supercontinuum and second harmonic generation on a single full integrated chip. The straightforward and high error-tolerant fabrication process combined with the corresponding large nonlinear coefficients of LN and ChG, make this a promising platform for variety of nonlinear optical applications such as optical frequency comb generation based on coherent SCG and stabilized by  $f$ -to- $2f$  CEO locking.

### 4.3 Efficient supercontinuum in hybrid nonlinear waveguides

Supercontinuum generation (SCG) is a process of spectral broadening induced by nonlinear optical effects. It has been used to generate broad-band optical frequency combs, which, depending on their spectral domain, can be used in applications such as optical spectroscopy [51], chemical sensing and microscopy [52], microwave photonics [53], astronomic spectrographs [54], and telecommunications [55]. Frequency combs are commonly generated through optical fiber and bulk technologies, but submicron integrated photonic waveguides generally possess superior properties for nonlinear effects in shorter lengths and with lower average power budgets. The high index contrast achievable in submicron waveguides allows tight mode confinement, giving rise to large electromagnetic fields and thus enhances the nonlinear effects. This has motivated a growing interest in nonlinear integrated photonics for the optical comb application [56, 57, 41]. Future developments could potentially lead to an increment of information rates, all-optical data processing, high-precision metrology and creation of broad spectral sources for on-chip optical spectroscopy, etc.

Optical frequency comb stabilization, by the  $f$ -to- $2f$  carrier-envelope offset (CEO) locking technique, requires at least an octave span of SCG and efficient second-harmonic generation (SHG) for CEO signal detection [41]. This implies the use of a highly third-order nonlinear medium to generate a broad frequency comb and a highly

second-order nonlinear material for frequency doubling. Furthermore, other applications can be envisioned by involving both nonlinearities, in which broad-band phase-matching conditions are fulfilled for SHG, such that a pre-broadened spectrum is extended to shorter wavelengths resulting in a multi-octave spectrum [58].

Among several material candidates [26], lithium niobate (LN) exhibits very strong second-order optical nonlinearity ( $\chi^{(2)}$  susceptibility) for SHG. Recent progress has created an opportunity for using thin films of LN in high-contrast ultracompact integrated waveguides [21]. To overcome the issue of phase mismatch between seed and converted guided optical waves, methods such as periodically-poled LN (PPLN) [23] and grating-assisted mode-shape modulation [25] can be applied to the high-contrast waveguides.

SCG at telecom wavelengths has been studied in a wide variety of highly third-order nonlinear ( $\chi^{(3)}$  susceptibility) materials. Over an octave-spanning SCG has been demonstrated in silicon nitride (SiN) [59], chalcogenide glass (ChG) [60, 61], silicon germanium [62], indium gallium phosphide [63] and silicon [64] waveguides. Even over two octaves has been reported in SiN [65] and aluminum nitride (AlN) [66]. AlN has the advantage of possessing both high quadratic and cubic nonlinearities, hence simultaneously achieving SHG and SCG on a single waveguide and measuring CEO frequency are feasible. However, both phenomena depend on waveguide dimensions and polarization, so the conditions for SHG may not be ideal for SCG and vice versa.

In this paper, we explore a solution that combines LN and ChG, with strong  $\chi^{(2)}$  and  $\chi^{(3)}$  nonlinearities, respectively, on a single chip. This cascaded integration, or nonlinear photonic circuit, allows us to optimize the two waveguides segments individually, leading to the desired wide spectrum for SCG and quasi-phase-matching (QPM) for efficient SHG [26], independent of each other.

### **4.3.1 Precepts of the hybrid platform for high-performance cascaded nonlinearities**

The first step towards the discussed nonlinear photonic circuits is to prove not only that integration is feasible between the two materials, but also the optical energy can be transferred from one to the other. To this end, we decouple a ChG channel waveguide from a LN thin film using a SiN rib (see the inset in Fig. 14). We have experimentally shown that the optical mode can reside within the ChG waveguide in the first segment, and subsequently be transferred via adiabatic tapers into the LN film, where it is laterally confined by the SiN rib [67]. In this previous work, we also demonstrated four-wave mixing (FWM) in the ChG waveguide, but the design was not suitable for wideband SCG. In the present paper, we focus on tailoring the structural and dispersion design for over an octave of SCG.

It is generally imperative to understand how the total group-velocity dispersion (GVD) and the pump wavelength affect the spectral broadening. Accordingly, if the pump pulse spectrum falls within the waveguide's normal dispersion regime, the broadening is mainly originated from self-phase modulation (SPM), and hence will be very limited in extension. Conversely, if the pulse is launched in the anomalous regime, additional broadening phenomena can be involved. Examples are optical Cherenkov radiation (OCR, responsible in dispersive waves), cascaded FWM, modulation instability (MI), cross-phase modulation (XPM) and soliton fission, all of which extend the spectral broadening further than the normal dispersion regime [68, 69]. It has also been shown that the more anomalous the dispersion, the narrower the bandwidth and vice versa [32]. Therefore, the total GVD has to be optimized for the pump wavelength to ideally fall in the anomalous regime and stays close to zero in an as large as possible wavelength range.

Coherence is another important characteristic to analyze in SCG, given that many applications depend upon it, including optical coherence tomography, ultrashort pulse compression, and high-precision frequency metrology. MI is a spontaneous gain process, such that the stronger it is, the less coherent the supercontinuum (SC). MI grows with input power, propagation length and in the strong anomalous dispersion [70], thus it is critical to minimize the impacts of these factors. OCR is a determinant broadening process in the anomalous regime, and it relies on phase-matching conditions only possible across zero-dispersion wavelengths. Accordingly, one-zero dispersion leads to one dispersive

wave, two-zero dispersion leads to two-dispersive waves and so on [68]. Considering that the total GVD is the addition of material and waveguide dispersions, it can be adjusted by either changing the involved materials or by modifying the waveguide structure or dimensions. In one creative design, for instance, attaining four-zero GVD - by adding a low-index slot within the waveguide - has been investigated [34, 35]. The concept of four-zero dispersion (FZD) provides a better basis for attaining the phase-matching conditions in OCR than waveguides with one- or two-zero dispersion wavelengths.

LN's highest nonlinear coefficient is at the crystalline  $Z$ -axis ( $d_{33} = 30$  pm/V), hence maximum conversion efficiency occurs when the electric field of the optical wave is collinear to this axis. The thin-film PPLN devices compatible with the current  $\chi^{(2)}$ - $\chi^{(3)}$  integration scheme [67] rely on  $Y$ -cut LN films, due to ease of electrode fabrication for poling. The direct implication is that the crystalline  $Z$ -axis is horizontally oriented, leading to higher performance for transverse-electric (TE) polarized input light. Therefore, all the simulations presented in this work are for the quasi-TE guided modes.

### 4.3.2 Dispersion calculations

The total GVD is calculated through the implementation of a fully-vectorial simulation in the commercial software COMSOL™, using its RF module to obtain the effective refractive index,  $n_{\text{eff}}$ , of the fundamental TE and TM modes for a sweep of wavelengths. The dispersion of different materials can be incorporated directly into the simulation. The

model accounts for the dispersion of every material involved. Most material dispersions were inputted by their Sellmeier equation [71], using the parameters listed in Table 1.

Table 1 Sellmeier coefficients for the materials involved in the nonlinear chip integration [31, 72, 73, 74].  $n^2(\lambda) = A + \frac{B_1\lambda^2}{\lambda^2-c_1} + \frac{B_2\lambda^2}{\lambda^2-c_2} + \frac{B_3\lambda^2}{\lambda^2-c_3}$ .

<i>Material</i>	<i>A</i>	<i>B<sub>1</sub></i>	<i>C<sub>1</sub> [μm<sup>2</sup>]</i>	<i>B<sub>2</sub></i>	<i>C<sub>2</sub> [μm<sup>2</sup>]</i>	<i>B<sub>3</sub></i>	<i>C<sub>3</sub> [μm<sup>2</sup>]</i>
<i>ChG Ge<sub>23</sub>Sb<sub>7</sub>S<sub>70</sub></i>	3.627	1.021	0.128	0.999	844.9	0	0
<i>LN ordinary</i>	1	2.673	0.018	1.229	0.059	12.61	474.6
<i>LN extra-ordinary</i>	1	2.980	0.020	0.598	0.066	8.954	416.1
<i>SiO<sub>2</sub></i>	1	0.696	0.005	0.408	0.013	0.897	97.93

Thin film SiN was characterized in our laboratory, using prism coupling method and fitting to the following Cauchy's equation.

$$n(\lambda) = 1.9283 + \frac{0.030385\mu\text{m}^2}{\lambda^2} - \frac{0.0037931\mu\text{m}^4}{\lambda^4} \quad (17)$$

Finally, the GVD is calculated through the second-order derivative of  $n_{\text{eff}}$  with respect to wavelength,  $\lambda$ , i.e., the dispersion parameter,  $D$ , expressed by

$$D = \frac{\lambda}{c} \left( \frac{d^2 n_{\text{eff}}}{d\lambda^2} \right), \quad (18)$$

where  $c$  is the speed of light in vacuum.

Using the cross-section of our previously fabricated nonlinear integrated chip [67] as a starting point, the SiN and LN dimensions were unchanged, while the dimension of the ChG waveguide was varied. After an exhaustive analysis of the TE mode evolution in the waveguide structures, we noticed that the inflection points in the GVD plot occur when the mode expands to the extent that it occupies the adjacent material regions (see Figure 14). From this attribution, it can be inferred that the slower the transition, the smaller the dispersion plot's curvature, and hence, by increasing the ChG dimensions, the dispersion becomes flatter. This leads to the hint that by adding adjacent high-index sections to the waveguide, the number of inflection points may increase, as it happens in the case of slot waveguides giving rise to FZD [34, 35].

In contrast to the dispersion of the TE modes, the transversal magnetic mode (TM) presents normal dispersion at  $1.55 \mu\text{m}$  for this tall structures. However, as discussed above, we are only interested in and aimed at the TE SC for further application involving LN waveguides, which possess the desired close-to-zero dispersion.

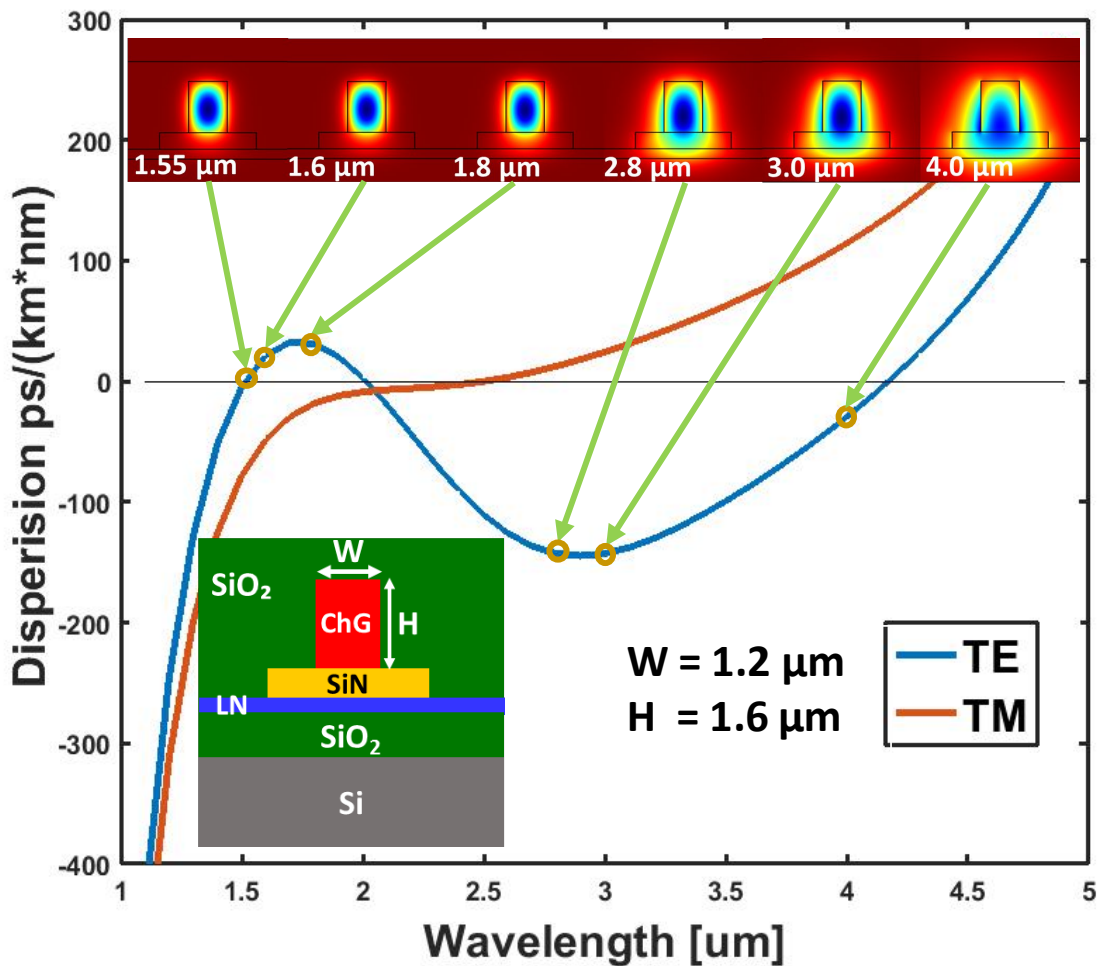


Figure 23: Detailed mode analysis showing how the inflection points of the GVD arise when the mode is expanded into adjacent regions for the TE polarization. TM dispersion is also shown for comparison.

We studied the effects of waveguide height variations on the dispersion, by fixing the width to 1.2  $\mu\text{m}$  and sweeping the height from 1.0 to 2.2  $\mu\text{m}$ . The taller the waveguides, the more the dispersion is pulled into the anomalous regime at shorter wavelengths (see Fig. 15(a)). Conversely, by fixing the height to 1.6  $\mu\text{m}$  and increasing the width results in flatter GVD, affecting the dispersion mostly around the 3- $\mu\text{m}$  wavelength along with a

major impact on the trend than height variation (Fig. 15(b)). This difference is attributed to the nature of the TE mode, which oscillates in parallel to the horizontal axis, hence having more interaction with the side boundaries than with the top and bottom material interfaces. A combination of these effects is used to get the desired GVD with small anomalous dispersion at 1.55  $\mu\text{m}$  wavelength, where the input pump will be centered.

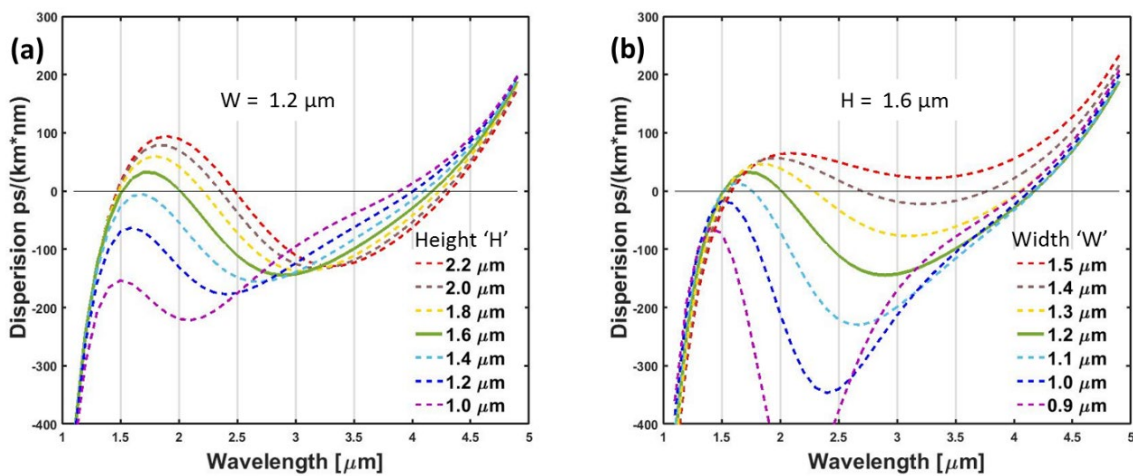


Figure 24: Dispersion plots for the ChG waveguide by (a) height and (b) width variations. The continuous line in green represents the chosen dispersion for SCG.

In Figs. 15(a) and 15(b), it is observed that the anomalous dispersion regime cannot be greatly extended into wavelengths below  $\sim 1.5 \mu\text{m}$  by only modifying the ChG dimensions, but it is enough to achieve the desired dispersion profile. Henceforward, we rely on OCR for wide spectrum broadening. However, in the case that further SCG extension to shorter wavelengths is desired, additional modifications can help, i.e., changing the SiN and LN dimensions or trying different cladding materials.

To summarize the design, the dimensions for the hybrid waveguides are as follows: a 300-nm thin-film LN on a SiO<sub>2</sub> substrate; a 3- $\mu\text{m}$ -wide, 500-nm-tall SiN rib loaded on LN; and a 1.2- $\mu\text{m}$ -wide, 1.6- $\mu\text{m}$ -tall ChG channel waveguide centered on top of the SiN rib. Under this condition we get the pump to fall closer to zero dispersion, and hence having smaller anomalous dispersion, conditions that lead to a wide SC. Similar general arguments and tradeoffs have been previously observed in the case of chalcogenide fibers [75].

### 4.3.3 Supercontinuum simulation

An in-house code that solves the general nonlinear Schrödinger equation (GNLSE) is employed to simulate the SC generated as the input pulse propagates through the waveguide, i.e. [76],

$$\frac{\partial A}{\partial z} + \frac{\alpha}{2}A - \sum_{k \geq 2} \frac{i^{k+1}}{k!} \beta^{(k)} \frac{\partial^k A}{\partial T^k} = i\gamma \left(1 + i\tau_s \frac{\partial}{\partial T}\right) |A|^2 A, \quad (19)$$

where  $A$  is the complex amplitude of the electric field of the optical mode,  $\alpha$  is the linear loss coefficient,  $\beta^{(k)}$  is the  $k^{\text{th}}$ -order dispersion, and  $\gamma$  is the nonlinear constant. Also,  $T = t - \beta^{(1)}z$  is the time transformed into a moving frame and  $\tau_s = 1/\omega_0$ , where  $\omega_0$  is the central angular frequency of the input pulse. Terms related to the Raman scattering can be also added to Eq. (19) [35]. However, the corresponding parameters have not been measured for the particular ChG composition used in this work; therefore, the associated

inelastic nonlinear effects are not included in the simulations. Nevertheless, it is expected that they merely cause a non-critical energy conversion in the resulting spectrum, and not seriously quench the desired elastic  $\chi(3)$  effects.

The simulations are adapted to the employed material properties and the estimated technical performances. The ChG waveguide propagation loss is set at 1 dB/cm, albeit lower values have been demonstrated in the past [49]. Nonlinear absorptions, due to two-photon and free-carrier absorptions, are generally considered to be negligible for the employed glass composition [31, 77]. High-order dispersion parameters were obtained by extending the Taylor series of the calculated second-order dispersion,  $\beta^{(2)} = \partial^2 \left( \frac{\omega}{c} n_{\text{eff}} \right) / \partial \omega^2$ , i.e.,

$$\beta^{(2)} = \beta^{(2)}(\Omega) + \beta^{(3)}(\Omega) \frac{\Omega}{1!} + \beta^{(4)}(\Omega) \frac{\Omega^2}{2!} + \dots, \quad (20)$$

keeping up to  $\beta^{(10)}$ , where  $\omega$  is the angular frequency and  $\Omega = \omega - \omega_0$ . An expression suitable for high-contrast hybrid waveguides was used for the calculation of  $\gamma$  [78]. That is,

$$\gamma = \frac{2\pi}{\lambda} \left( \frac{n_{\text{eff}}}{n_{\text{core}}} \right)^2 \frac{n_2^{\text{avg}}}{A_{\text{eff}}}, \quad (21)$$

where  $n_{\text{core}}$  is the refractive index of the nonlinear guiding material,  $A_{\text{eff}}$  is the effective area of the propagating mode,  $n_2^{\text{avg}}$  is an average nonlinear refractive index that accounts for all the involved materials. If the nonlinearity is much larger for the core than the adjacent regions, then  $n_2^{\text{avg}}$  can be approximated as

$$n_2^{\text{avg}} = n_2 \frac{n_{\text{core}}^4 \iint_{\text{NL}} |E(x, y)|^4 dx dy}{\iint_{-\infty}^{\infty} |E(x, y)|^4 n(x, y)^4 dx dy}, \quad (22)$$

and  $A_{\text{eff}}$  is calculated using

$$A_{\text{eff}} = \frac{(\iint_{-\infty}^{\infty} n(x, y)^2 |E(x, y)|^2 dx dy)^2}{\iint_{-\infty}^{\infty} n(x, y)^4 |E(x, y)|^4 dx dy}. \quad (23)$$

The nonlinear refractive index of the ChG composition is  $n_2 = 3.71 \times 10^{-18} \text{ m}^2/\text{W}$  [31], thus, the final calculated value of the nonlinear constant is  $\gamma = 10.53 \text{ W}^{-1} \text{ m}^{-1}$ . The effective area at the 1.55  $\mu\text{m}$  wavelength, for instance, is  $1.27 \mu\text{m}^2$ .

The input beam is a *sech*<sup>2</sup> pulse with a waist of 250-fs full width at half maximum (FWHM), and peak power of 100 W. This means an energy of only 25 pJ, which is adequate for octave-spanning SCG. Indeed, the simulations shown in Figure 22 confirm that  $\sim 1.27$ -octave SC is feasible with such low energy pulses, after 40 mm of propagation in the discussed waveguide design. The spectrum extends from  $\sim 1150$  to  $> 2800$  nm at 20 dB below maximum power. A wider SC output spectrum can be achieved, in principle, by employing shorter-duration input pulses. However, the validity of the employed GNLSE, Eq. (3), becomes questionable for such extremely short pulses [79], and it is thereby not explored further here.

In Fig. 16(a), it is clear that the pulse initially broadens symmetrically through SPM. Once it reaches  $\sim 20$  mm propagation length, pulse compression is observed in the time domain (Fig. 16(b)), which leads to a rapid spectrum broadening. At this point, dispersive

waves become apparent at both sides of the central spectrum, and they continue growing with further propagation, pretty much defining the SC limits. After the pulse starts dispersing in time, the optical fields lose their intensity and the spectrum ceases to stretch. This shows the importance of choosing the appropriate waveguide length for the desired functionality. For example, if the waveguide is truncated at 20 mm, a compressed pulse is attainable.

It is also noted that  $f$ -to- $2f$ CEO locking is an interference technique, so it requires SCG with decent temporal coherence. Keeping a short propagation distance and low input power are measures to prevent low coherence broadening effects, such as MI, which is very sensitive to noise, leading to low correlation between consecutive pulses.

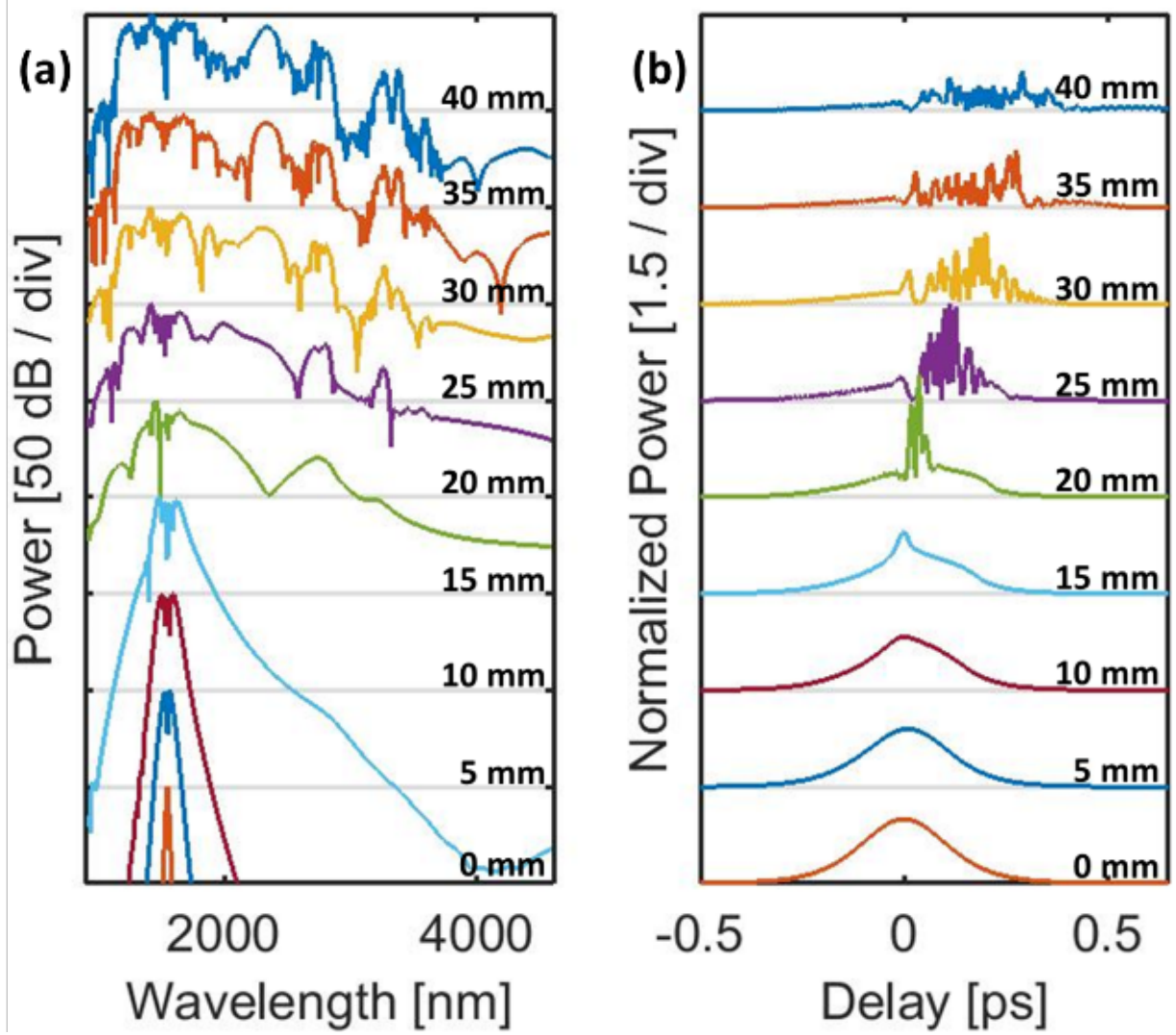


Figure 25: Pulse evolution in wavelength (a) and time (b) domains, after 40 mm propagation of TE modes in hybrid ChG waveguides. It is evident how the pulse starts braking in the time domain after 15 mm, progressing to high compression at 20 mm. The supercontinuum finally extends from  $\sim 1150$  to  $> 2800$  nm at 20 dB below maximum, i.e., over 1.25 octave.

#### 4.3.4 Fabrication

The next milestone towards the demonstration of cascaded  $\chi^{(2)}$  and  $\chi^{(3)}$  nonlinearities is to prove that the optical mode can be transferred efficiently from ChG to LN. This is achievable by careful design of an adiabatic tapered mode-converter on the top ChG waveguide, as depicted in Fig. 17(c). As the ChG waveguide is adiabatically tapered, the mode shape continuously evolves, creating a smooth mode translation. The decrease of ChG area leads to a local decrease of the effective refractive index, consequently pushing the mode down to the high index LN waveguide. We studied the coupling efficiency for a sweep of taper lengths with the use of the commercial software Lumerical™ MODE Solutions. Presented in Fig. 16(d), we find that keeping the taper length above 100  $\mu\text{m}$  will grant a high coupling efficiency close to 100% at an example wavelength of 2.4  $\mu\text{m}$ , corresponding to the long-wavelength tail of the SC spectrum, as required for the  $f$ -to- $2f$  CEO detection application. Figure 17(a) shows the mode transition obtained for a 1-mm-long taper. Figures 17(b) and (e) are transversal modal cross-sections at the beginning and end of the structure layout in Fig. 17(c). It shows how the optical mode is initially restrained in ChG and then lands in the LN rib-loaded waveguide, with most of its energy contained in the thin-film LN, where second-order nonlinear processes can occur. As we have shown in our previous work, the discussed tapered mode-converters are very broadband [67]. In this present design, the 3-dB bandwidth extends from  $\sim 1.0 \mu\text{m}$  to above 3.5  $\mu\text{m}$  wavelength (not shown).

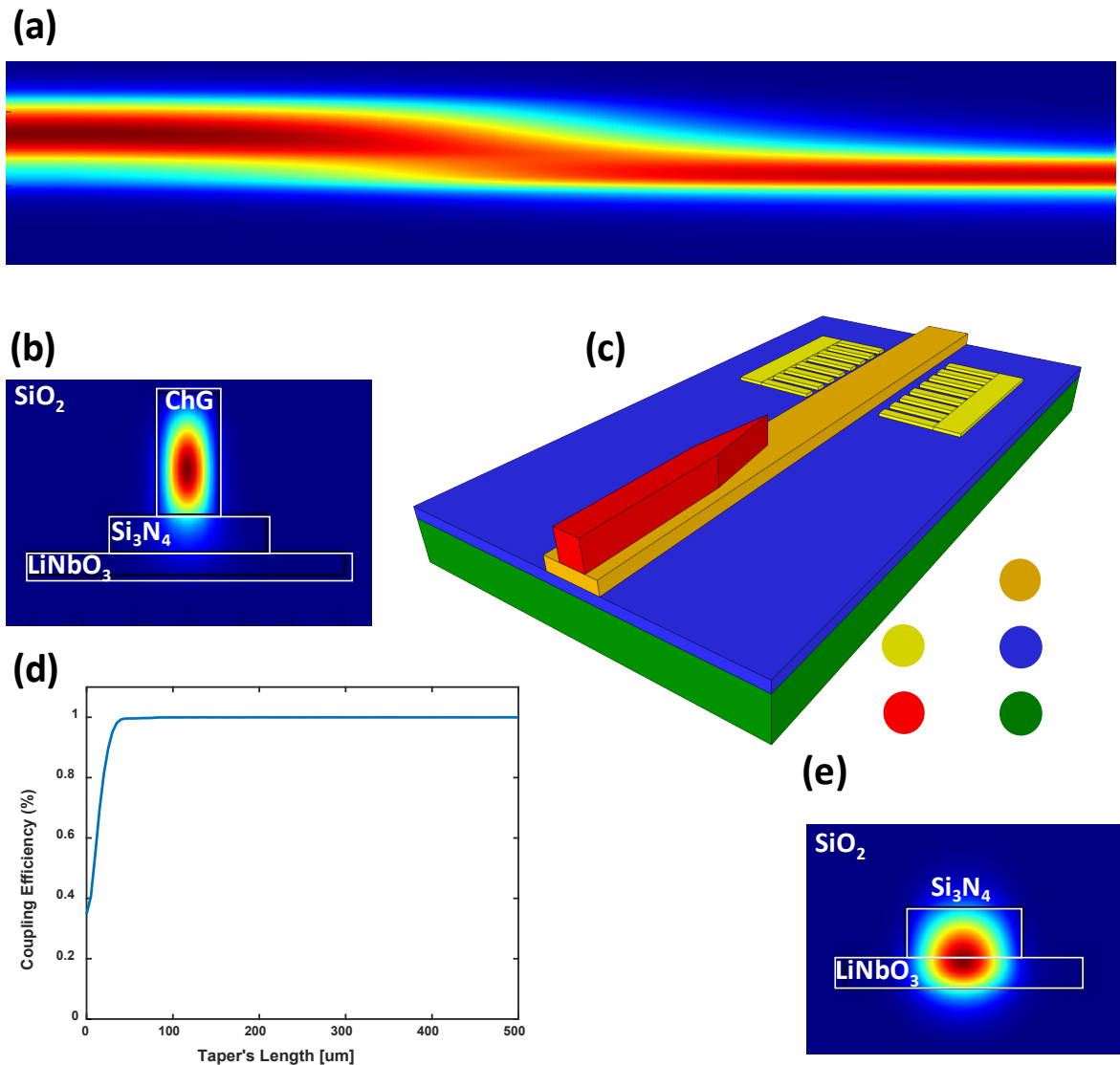


Figure 26: (a) Quasi-TE optical mode being coupled from ChG to LN; (b) Fundamental mode distribution in ChG waveguide; (c) Fully integrated nonlinear chip for cascaded  $\chi^{(2)}$  and  $\chi^{(3)}$  effects; (d) Coupling efficiency through a sweep of taper lengths; (e) Fundamental mode distribution in LN waveguide.

As schematically shown in Fig. 17(c), the LN thin film can be periodically poled to achieve QPM [21] and hence high SHG conversion efficiency, for CEO signal detection [41].

Another potential application is to engineer the LN poling condition for broad-band QPM,

stretching the SC spectrum into shorter wavelengths, potentially with a span of multiple octaves [58].

The fabrication process of the current cascaded nonlinear devices is very similar to our previous experimental work [67]. Starting with a thin-film LN bonded on SiO<sub>2</sub>, SiN is deposited on top. The SiN layer is then patterned and etched. Subsequently, a ChG film is similarly deposited, patterned and etched. Finally, SiO<sub>2</sub> is deposited to passivate the waveguides and attain the complete nonlinear photonic circuit.

## CHAPTER 5: FUTURE WORK

Further characterization of nonlinear material thin films is indispensable for its application in nonlinear integrated photonics. Thus, it is my hope that the research presented in this thesis will encourage the future study of thin films optical properties. Fabrication techniques and processes affect the materials, sometimes changing stoichiometry or density, for example. Hence, using bulk material properties for integrated photonics simulations is a mere approximation,

Ongoing fabrication will lead to experimental measurements of efficient second- and third-order nonlinear processes happening on a single heterogeneous waveguide. This will only be a first step through more complex heterogeneous integration of nonlinear materials.

For instance, self-referenced frequency combs are in the aim of nonlinear integrated optics, due to their wide range of applications. From atomic clocks, to space spectroscopy, every high precision frequency measurement requires a fine self-referenced frequency comb, which would act as a frequency "ruler", and developing this technology on micro-chips will definitely bring technology miniaturization to a next level.

The preferred method for self-referencing a frequency comb is through the interference of a second harmonic converted signal from a low frequency line of the frequency comb, with its closest comb-line. The interference of these two signal will produce a beat note

at considerable lower frequency than any comb frequency, converting a terahertz signal into a microwave signal, which can be easily detected by a fast photo-diode. This beat signal turns out to be identical to the carrier-envelope offset (CEO) frequency, which added to the laser's repetition rate, becomes the exact spacing between comb lines. Evidently, this application requires at least one octave of frequency comb, along with SHG. We demonstrated second- and third-order nonlinear effects happening in independent waveguides and we demonstrated these waveguides integrability. Moreover, we proved numerically that the integrated device can generate the required octave supercontinuum comb, and we know that SHG in thin-film lithium niobate can be adjusted to efficiently double any specific frequency. Thus, the next step is to put this together on a single chip and see both effects happening together. If the pulsed pump turns out to be highly coherent, we may be able to detect the CEO frequency directly from the output, in a device such as the one depicted in Figure 26(c), This can be done using a band pass filter or with the help of a dispersive grating.

Otherwise, to get a higher signal to noise ratio, beam-splitters would be added to the waveguides, in order to add and possibly control the phase of one of the interfering signals. Adjusting this phase will help us to reach high temporal coherence, leading to higher signal to noise ratio. A picture of the proposed integrated chip is depicted in Figure 27.

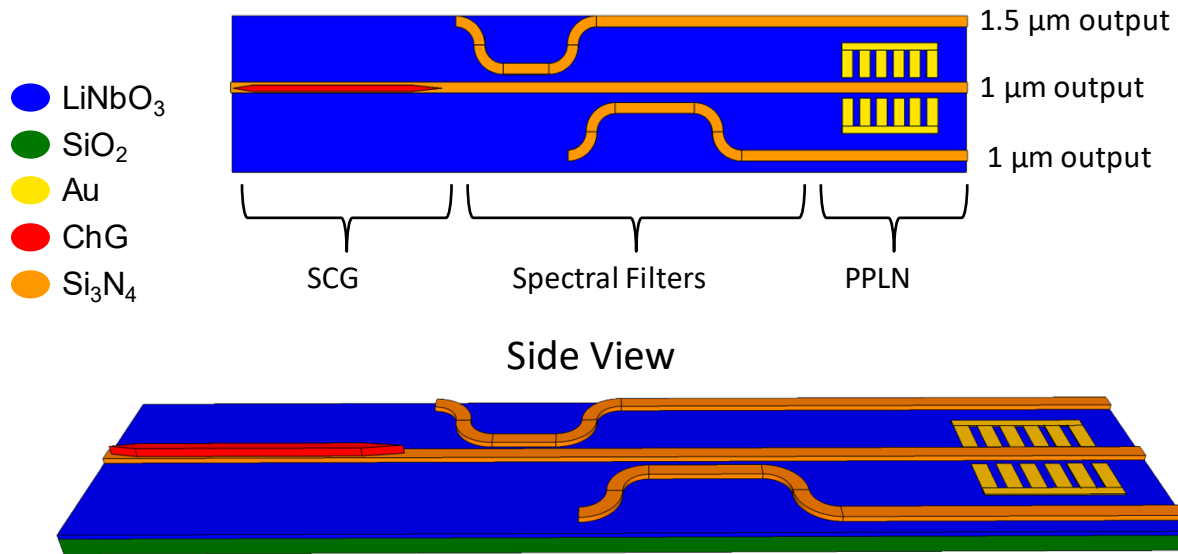


Figure 27: Top view and side view of the proposed fully integrated nonlinear chip, which includes a ChG channel waveguide for supercontinuum, beam splitters and PPLN [80].

Alternatively, in a slightly more complex device, an integrated modulator would help to adjust the interfering beams on-chip, and collect a single output.

## CHAPTER 6: CONCLUSION

Silicon photonics monolithic integration is convenient in fabrication and integrability, however, an ideal fully integrated photonic circuit would include active optics, passive waveguides, integrated laser sources and photodetectors. Nor silicon or any other material is attributed with superior performance in every single optical aspect, therefore, heterogeneous integration becomes not only helpful, but necessary for the future development of integrated photonics.

Throughout this work, we described some experiments for characterization of chalcogenide waveguide's losses using ring resonators. Dispersion was calculated for different ChG waveguide structures, mainly channel waveguides and slot waveguides. Although Slot waveguides is capable of display a very flat four-zero dispersion profile, fabrication would be more complicated, and nevertheless, channel waveguides were good enough to get an octave supercontinuum.

SHG generation was discussed for lithium niobate waveguides, and two methods to achieve efficient conversion were presented. Periodically poling will enhance conversion efficiency more effectively than mode-shape modulation, however, mode shape modulation is applicable to any material which not necessarily rely on ferroelectric effect.

Finally a final integrated chip was modeled and proved numerically to achieve over an octave supercontinuum. This, combined with selective SHG, is a first step for on-chip self-referenced frequency comb, through  $f$ -to- $2f$  interferometry.

## **APPENDIX A- FABRICATION METHODOLOGY**

This appendix is a quick guide through the fabrication of the integrated nonlinear waveguide, including electrodes for periodic polling.

1. Start with bonded lithium niobate on silicon dioxide wafer.
2. Clean thoroughly using acetone, isopropanol and water in that order. I recommend to direct the solvents stream to the sample, hitting the tweezer at last. If you hit the tweezer first, dirt will be propelled to the rest of the sample.
3. Dehydrate on the hot plate at 90 °C for one minute.
4. Spin ZEP 520-A resist at 3000 rpm on a single step (no ramp up or down), and bake at 180 °C for 3 minutes.
5. Expose markers and electrodes with e-beam lithography.
6. Develop in Xylene for two minutes, shaking gently and soak the sample into isopropanol immediately after.
7. Blow gently and verify development. It may require a bit longer development.
8. Deposit 20 nm of chromium followed by 100 nm of gold.
9. After deposition, soak sample into NMP (1-methyl 2-pyrrolidinone) solvent at 90 °C and wait for lift-off to happen.
10. Clean with water, dehydrate at 90°C for one minute and prepare it for ChG deposition through thermal evaporation.
11. Deposit 100 nm of ChG.

12. Spin ZEP 520-A resist at 3000 rpm on a single step (no ramp up or down), and bake at 180 °C for 3 minutes.
13. Use gold markers for alignment of the second e-beam lithography layer.
14. Develop in Xylene for two minutes, shaking gently and soak the sample into isopropanol immediately after.
15. Fully etch the 100 nm of ChG using 2 sccm of CL<sub>2</sub> flow and 40 sccm of Argon recipe. (Rate around 300 nm/min).
16. Deposit 1 μm of ChG through thermal evaporation.
17. ChG absorbs the visible, which is used by the e-beam tool to locate electrodes. Therefore markers have to be uncovered. This can be done by rough alignment to the sample's center and e-beam exposure of the marker's area, followed by development and full etching. Or covering the markers during ChG deposition.
18. Once markers are uncovered, proceed to spin ZEP 520-A resist at 3000 rpm on a single step (no ramp up or down), and bake at 180 °C for 3 minutes.
19. Use gold markers for alignment of the third e-beam lithography layer.
20. Develop in Xylene for two minutes, shaking gently and soak the sample into isopropanol immediately after.
21. Fully etch the 1 μm of ChG using 2 sccm of CL<sub>2</sub> flow and 40 sccm of Argon recipe. (Rate around 300 nm/min).

22. Soak the sample into NMP (1-methyl 2-pyrrolidinone) solvent at 90 °C to clean every resist residue.
23. Passivate preferably with sputtered silicon dioxide, which is a cold deposition and prevents from stress damages.
24. Dice, cleave and polish to start measurements.

## **APPENDIX B-MATLAB CODES**

This is the collection of codes for dispersion and supercontinuum calculations.

1. Starting with the code for group velocity dispersion calculations, which in addition calculates up to ten higher order dispersions.

```
clear all
% import COMSOL data from a txt file
fileToRead1='chgsinln_chg700h4000w_ln300h_TE_richardsondispersion_TM.txt';
data=importdata(fileToRead1, ' ');
c_0 = 299792458;
% parsing the text file
lam = data(:,1);
ll = length(lam);
lam = lam(4:ll);
lam = str2double(lam);
n_eff = data(:,2);
n_eff = n_eff(4:ll);
n_eff = str2double(n_eff);

n_total = n_eff;

% use finite difference scheme to calculate the dispersion
%  $D = - \frac{1}{c} \frac{d^2 n}{d\lambda^2}$ 
% assumes that  $\Delta \lambda$  step size in lam is constant

d_lam = lam(2) - lam(1);
NN = length(lam);
dispersion_fd = zeros(NN-2,1);
lam_fd = lam;
lam_fd(1) = []; % we are using a centered finite difference scheme
lam_fd(NN-1) = [];

for k = 2:(NN-1)
    dispersion_fd(k-1) = (n_total(k-1) + n_total(k+1) - 2.0
*n_total(k))/d_lam^2;
end
dispersion_fd = - lam_fd/c_0.*dispersion_fd*1.0e6; %since lam is in [um]

%fig1 = figure();
line = zeros(NN-2,1);

plot(lam_fd,dispersion_fd*1e6,'r'); % 1e6 covert to ps/(km nm)
hold on
plot(lam_fd,line,'k');
xlabel('Wavelength [um]');
ylabel('Disperision ps/(km*nm)');
```

```

xlim([1 5])
ylim([-400 300])

%% This next part is to get beta in terms of omega
omega_center = 2*pi*c_0./1.55*1e6;
omega1 = 2*pi*c_0./lam*1e6;

omega = flip(omega1);%this and next line just to sort from smaller to bigger
neff_omega = flip(n_eff);

format longEng
beta_om = omega.*neff_omega/c_0;

[poli_beta,~,mu] = polyfit(omega, beta_om,7);%fit for beta1

omegapo = (5:0.001:19)*1e14;%to take derivative
f = polyval(poli_beta,omegapo, [],mu);
d_omega = omegapo(2) - omegapo(1);
ii = length(omegapo);
betatwo = zeros(ii-2,1);
omega_fd = omegapo;
omega_fd(1) = []; % we are using a centered finite difference scheme
omega_fd(NN-1) = [];

for k = 2:(ii-1)
    betatwo(k-1,1) = (f(k-1) +f(k+1) - 2.0 *f(k))/d_omega^2;
end

domega = omega_fd - omega_center;

p = polyfit(domega', betatwo,8);%It gives me only tailor parameters, so need
to be converted to actual betas
flip(p')

```

## 2. Convert dispersion to required units:

```

%% Adjust polynomial parameters to actual betas in units [ps^2/m, ps^3/m ...]

beta2_poly_coefficients = [-72.4777832597252e-027
    892.231334071375e-042
   -779.478294564821e-057
    984.021145851833e-072
    541.026387044728e-087
   -1.83809684196799e-099
   -532.052128175681e-120
   -135.519734674070e-135
    638.122138428944e-150];
beta2 = zeros(length(beta2_poly_coefficients),1);

```

```

for kk = 1:length(beta2_poly_coefficients)
    %note that coeff. come from polynomial d^2/dw^2 B = A1 + A2 w ....
    % w is dOmega from Taylor expansion centered around omega_carrier
    beta2(kk,1) = beta2_poly_coefficients(kk)*factorial(kk-1)*(1e12)^(kk+1);
end

beta2

%% Getting dispersion parameter
wlam = [0.900:0.001:5.000];%um
c_0 = 299792458;
womega_center = 2*pi*c_0./(1.55*1e-6);
womega_del = 2*pi*c_0./(wlam*1e-6)-womega_center;%Hz[1/s]

ff = length(beta2);
gg = length(womega_del);
D = zeros(gg,1);

for ll = 1:gg
    for ii = 1:ff
        D(ll,1) = D(ll,1) + beta2(ii,1)/factorial(ii+1)*(womega_del(ll)*1e-
12)^(ii+1);
    end
end
figure
plot(wlam,D)

```

### 3. Non linear Schrodinger equation, function defined for supercontinuum generation solver:

```

function [Z, AT, AW, W] = gnlse(T, A, w0, gamma, betas, ...
    loss, fr, RT, flength, nsaves)
% Propagate an optical field using the generalised NLSE
% This code integrates Eqs. (3.13), (3.16) and (3.17).
% For usage see the exampe of test_Dudley.m (below)
% Written by J.C. Travers, M.H. Frosz and J.M. Dudley (2009)
% Please cite this chapter in any publication using this code.
% Updates to this code are available at www.scgbook.info
n = length(T); dT = T(2)-T(1); % grid parameters
V = 2*pi*(-n/2:n/2-1)'/(n*dT); % frequency grid
alpha = log(10.^(loss/10)); % attenuation coefficient
B = 0;
for i = 1:length(betas) % Taylor expansion of betas
    B = B + betas(i)/factorial(i+1).*V.^(i+1);
end
L = 1i*B - alpha/2; % linear operator
if abs(w0) > eps % if w0>0 then include shock
    gamma = gamma/w0;
    W = V + w0; % for shock W is true freq
else
    W = 1; % set W to 1 when no shock

```

```

end
RW = n*ifft(fftshift(RT.)); % frequency domain Raman
L = fftshift(L); W = fftshift(W); % shift to fft space
% === define function to return the RHS of Eq. (3.13)
function R = rhs(z, AW)
    AT = fft(AW.*exp(L*z)); % time domain field
    IT = abs(AT).^2; % time domain intensity
    if (length(RT) == 1) || (abs(fr) < eps) % no Raman case
        M = ifft(AT.*IT); % response function
    else
        RS = dT*fr*fft(ifft(IT).*RW); % Raman convolution
        M = ifft(AT.*((1-fr).*IT + RS)); % response function
    end
    R = li*gamma*W.*M.*exp(-L*z); % full RHS of Eq. (3.13)
end
% === define function to print ODE integrator status
function status = report(z, y, flag) %
    status = 0;
    if isempty(flag)
        fprintf('%05.1f %% complete\n', z/flength*100);
    end
end
% === setup and run the ODE integrator
Z = linspace(0, flength, nsaves); % select output z points
% === set error control options
options = odeset('RelTol', 1e-5, 'AbsTol', 1e-12, ...
    'NormControl', 'on', ...
    'OutputFcn', @report);
[Z, AW] = ode45(@rhs, Z, ifft(A), options); % run integrator
% === process output of integrator
AT = zeros(size(AW(1,:)));
for i = 1:length(AW(:,1))
    AW(i,:) = AW(i, :).*exp(L.*Z(i)); % change variables
    AT(i,:) = fft(AW(i, :)); % time domain output
    AW(i,:) = fftshift(AW(i, :))./dT; % scale
end
W = V + w0; % the absolute frequency grid
end

```

#### 4. Supercontinuum generation solver:

```

n = 2^11; % number of grid points
twidth = 8;%10; % width of time window [ps]
c = 299792458*1e9/1e12; % speed of light [nm/ps]
wavelength = 1550; % reference wavelength [nm]
w0 = (2.0*pi*c)/wavelength; % reference frequency [2*pi*THz]
T = linspace(-twidth/2, twidth/2, n); % time grid
% === input pulse
power = 100; % peak power of input [W]
t0 = 0.0284*5; % duration of input [ps]
A = sqrt(power)*sech(T/t0); % input field [W^(1/2)]
% === fibre parameters

```

```

flength = 0.045;           % fibre length [m]
% betas = [beta2, beta3, ...] in units [ps^2/m, ps^3/m ...]
betas = [-56.9882412259770e-003
        555.578184351746e-006
        325.652028753866e-009
        -10.8531796541622e-009
        133.122043361845e-012
        -532.388346712866e-015
        19.7743806755433e-018
        35.1462562273062e-021
        -1.32825106255565e-021]';
gamma = 10.53;             % nonlinear coefficient [1/W/m]
loss = 100;                % loss [dB/m]
% === Raman response
fr = 0.0;% 0.031;%0.18;%   % fractional Raman contribution
%tau1 = 0.0155; tau2 = 0.2305;
%RT = (tau1^2+tau2^2)/tau1/tau2^2*exp(-T/tau2).*sin(T/tau1);
%RT(T<0) = 0;              % heaviside step function
RT = 0.0;
%RT = RT/trapz(T,RT); % normalise RT to unit integral
% === simulation parameters
nsaves = 451;             % number of length steps to save field at
% propagate field
[Z, AT, AW, W] = gnlse(T, A, w0, gamma, betas, loss, ...
                      fr, RT, flength, nsaves);
% === plot output
fig1 = figure();%figure();
lIW = 10*log10(abs(AW).^2); % log scale spectral intensity
mlIW = max(lIW');         % max value, for scaling plot
WL = 2*pi*c./W;% iis = (WL>400 & WL<1350); % wavelength grid
subplot(1,2,1);
%pcolor(WL(iis), Z, lIW(:,iis)); % plot as pseudocolor map
%caxis([mlIW-40.0, mlIW]); xlim([900,2350]); shading interp;
iis = (WL>700 & WL<6000);
%normalize = max(lIW(351,iis));
plot(WL(iis)/1000, lIW(401,iis)-mlIW(401));
xlim([0.900,4.600]);
ylim([-450,0])
xlabel('Wavelength [nm]'); ylabel('Power [dBc]');
hold on
plot(WL(iis)/1000, lIW(351,iis)-mlIW(351)-50);%best
plot(WL(iis)/1000, lIW(301,iis)-mlIW(301)-100);
plot(WL(iis)/1000, lIW(251,iis)-mlIW(251)-150);
plot(WL(iis)/1000, lIW(201,iis)-mlIW(201)-200);
plot(WL(iis)/1000, lIW(151,iis)-mlIW(151)-250);
plot(WL(iis)/1000, lIW(101,iis)-mlIW(101)-300);
plot(WL(iis)/1000, lIW(51,iis)-mlIW(51)-350);
plot(WL(iis)/1000, lIW(1,iis)-mlIW(1)-400);

%figure ();
lIT = abs(AT).^2; % log scale temporal intensity
mlIT = max(lIT');   % max value, for scaling plot
normalize2 = mlIT(1);
subplot(1,2,2);
plot(T(iis), lIT(401,iis)/normalize2);
xlim([-0.5,1.0]);
ylim([-12.5,1.5])

```

```
xlabel('Delay [ps]'); ylabel('Power [Watts]');
hold on
plot(T(iis), lIT(351,iis)/normalize2-1.5);
plot(T(iis), lIT(301,iis)/normalize2-3);
plot(T(iis), lIT(251,iis)/normalize2-4.5);
plot(T(iis), lIT(201,iis)/normalize2-6);
plot(T(iis), lIT(151,iis)/normalize2-7.5);
plot(T(iis), lIT(101,iis)/normalize2-9);
plot(T(iis), lIT(51,iis)/normalize2-10.5);
plot(T(iis), lIT(1,iis)/normalize2-12);
set(findall(fig1, '-property', 'LineWidth'), 'LineWidth', 2);
set(findall(fig1, '-property', 'FontSize'), 'FontSize', 24);
```

## **APPENDIX C-COPYRIGHT PERMISSIONS**



# RightsLink®

[Home](#)
[Create Account](#)
[Help](#)


**Title:** Cascaded Integration of Optical Waveguides With Third-Order Nonlinearity With Lithium Niobate Waveguides on Silicon Substrates

**Author:** Amirmahdi Honardoost

**Publication:** IEEE Photonics Journal

**Publisher:** IEEE

**Date:** June 2018

Copyright © 2018, IEEE

#### LOGIN

If you're a [copyright.com](#) user, you can login to RightsLink using your [copyright.com](#) credentials. Already a RightsLink user or want to [learn more?](#)

### Thesis / Dissertation Reuse

**The IEEE does not require individuals working on a thesis to obtain a formal reuse license, however, you may print out this statement to be used as a permission grant:**

*Requirements to be followed when using any portion (e.g., figure, graph, table, or textual material) of an IEEE copyrighted paper in a thesis:*

- 1) In the case of textual material (e.g., using short quotes or referring to the work within these papers) users must give full credit to the original source (author, paper, publication) followed by the IEEE copyright line © 2011 IEEE.
- 2) In the case of illustrations or tabular material, we require that the copyright line © [Year of original publication] IEEE appear prominently with each reprinted figure and/or table.
- 3) If a substantial portion of the original paper is to be used, and if you are not the senior author, also obtain the senior author's approval.

*Requirements to be followed when using an entire IEEE copyrighted paper in a thesis:*

- 1) The following IEEE copyright/ credit notice should be placed prominently in the references: © [year of original publication] IEEE. Reprinted, with permission, from [author names, paper title, IEEE publication title, and month/year of publication]
- 2) Only the accepted version of an IEEE copyrighted paper can be used when posting the paper or your thesis on-line.
- 3) In placing the thesis on the author's university website, please display the following message in a prominent place on the website: In reference to IEEE copyrighted material which is used with permission in this thesis, the IEEE does not endorse any of [university/educational entity's name goes here]'s products or services. Internal or personal use of this material is permitted. If interested in reprinting/republishing IEEE copyrighted material for advertising or promotional purposes or for creating new collective works for resale or redistribution, please go to [http://www.ieee.org/publications\\_standards/publications/rights/rights\\_link.html](http://www.ieee.org/publications_standards/publications/rights/rights_link.html) to learn how to obtain a License from RightsLink.

If applicable, University Microfilms and/or ProQuest Library, or the Archives of Canada may supply single copies of the dissertation.

[BACK](#)
[CLOSE WINDOW](#)

Copyright © 2019 [Copyright Clearance Center, Inc.](#) All Rights Reserved. [Privacy statement](#). [Terms and Conditions](#). Comments? We would like to hear from you. E-mail us at [customercare@copyright.com](mailto:customercare@copyright.com)

6/24/2019

Mail - gcamacho@Knights.ucf.edu

## RE: reprint permission for PhD dissertation

pubscopyright <copyright@osa.org>

Mon 6/24/2019 4:52 PM

To: Guillermo Fernando Camacho Gonzalez <gcamacho@Knights.ucf.edu>; pubscopyright <copyright@osa.org>;

Dear Guillermo Fernando Camacho Gonzalez,

Thank you for contacting The Optical Society.

For the use of material from [1] Guillermo Fernando Camacho Gonzalez, Marcin Malinowski, Amirmahdi Honardoost, and Sasan Fathpour, "Design of a hybrid chalcogenide-glass on lithium-niobate waveguide structure for high-performance cascaded third- and second-order optical nonlinearities," *Appl. Opt.* 58, D1-D6 (2019):

Because you are the author of the source paper from which you wish to reproduce material, OSA considers your requested use of its copyrighted materials to be permissible within the author rights granted in the Copyright Transfer Agreement submitted by the requester on acceptance for publication of his/her manuscript. If the entire article is being included, it is requested that the **Author Accepted Manuscript** (or preprint) version be the version included within the thesis and that a complete citation of the original material be included in any publication. This permission assumes that the material was not reproduced from another source when published in the original publication.

The **Author Accepted Manuscript** version is the preprint version of the article that was accepted for publication but not yet prepared and/or formatted by The Optical Society or its vendors.

For the use of material from [2] G. F. Camacho-Gonzalez, M. Malinowski, A. Honardoost, and S. Fathpour, "Above-Octave Supercontinuum Generation in a Hybrid Nonlinear Waveguide for On-Chip Cascaded Third- and Second-Order Nonlinear-Optic Applications," in *Conference on Lasers and Electro-Optics, OSA Technical Digest (Optical Society of America, 2019)*, paper JTU2A.88:

OSA only has copyright for the compilation of the conference proceedings, not the individual papers themselves. As the authors retain copyright to the individual paper, an OSA credit statement is not needed, although we do request a complete citation be included in any publication or adjacent to any posting.

While your publisher should be able to provide additional guidance, OSA prefers the below citation formats:

For citations in figure captions:

[Reprinted/Adapted] with permission from ref [x], [Publisher]. (with full citation in reference list)

For images without captions:

Journal Vol. #, first page (year published) An example: *Appl. Opt.* 58, D1 (2019)

Please let me know if you have any questions.

Kind Regards,

Rebecca Robinson

<https://outlook.office.com/owa/?realm=knights.ucf.edu&path=/mail/inbox>

1/2

## LIST OF REFERENCES

- [1] E. Sarasin, "Jean Daniel Colladon," *Nature*, vol. 48, no. 1243, pp. 396-397, 1893.
- [2] J. Hecht, "Illuminating the origin of light guiding," *Optics and Photonics News*, vol. 10, no. 10, p. 26, 1999.
- [3] K. C. Kao and G. A. Hockham, "Dielectric-fibre surface waveguides for optical frequencies," *In Proceedings of the Institution of Electrical Engineers*, vol. 113, no. 7, pp. 1151-1158, 1966.
- [4] G. P. Agrawal, *Fiber-optic communication systems*, John Wiley & Sons, 2012.
- [5] B. Jalali and S. Fathpou, "Silicon Photonics," *J. Lightwave Technol.*, no. 24, pp. 4600-4615, 2006.
- [6] B. Jalali, S. Yegnanarayanan, T. Yoon, T. Yoshimoto, I. Rendina and F. Coppinger, "Advances in silicon-on-insulator optoelectronics," *IEEE Journal of selected topics in Quantum Electronics* 4, no. 6, pp. 938-947, 1998.
- [7] M. Lipson, "Guiding, modulating, and emitting light on silicon-challenges and opportunities," *Journal of Lightwave Technology* 23, no. 12, p. 4222, 2005.
- [8] D. J. Lockwood and L. Pavesi, *Silicon Photonics III*, Berlin, Heidelberg: Springer, 2004, pp. 1-50.
- [9] R. Soref, "The past, present, and future of silicon photonics," *IEEE Journal of selected topics in quantum electronics* 12, no. 6, pp. 1678-1687, 2006.
- [10] B. Jalali, "Can silicon change photonics?," *physica status solidi (a)* 205, no. 2, pp. 213-224, 2008.
- [11] L. Thylén and L. Wosinski, "Integrated photonics in the 21st century," *Photonics Research* 2, no. 2, pp. 75-81, 2014.

- [12] S. Fathpour, "Emerging heterogeneous integrated photonic platforms on silicon," *Nanophotonics* 4, no. 1, pp. 143-164, 2015.
- [13] S. Khan, M. A. Baghban and S. Fathpour, "Electronically tunable silicon photonic delay lines," *Optics express* 19, no. 12, pp. 11780-11785, 2011.
- [14] S. Khan and S. Fathpour, "Complementary apodized grating waveguides for tunable optical delay lines," *Optics express* 20, no. 18, pp. 19859-19867, 2012.
- [15] S. Khan and S. Fathpour, "Demonstration of complementary apodized cascaded grating waveguides for tunable optical delay lines," *Optics letters* 38, no. 19, pp. 3914-3917, 2013.
- [16] S. Khan and S. Fathpour, "Demonstration of tunable optical delay lines based on apodized grating waveguides," *Optics Express* 21, no. 17, pp. 19538-19543, 2013.
- [17] S. Khan, J. Chiles, J. Ma and S. Fathpour, "Silicon-on-nitride waveguides for mid- and near-infrared integrated photonics," *Applied Physics Letters* 102, no. 12, p. 121104, 2013.
- [18] J. Chiles, S. Khan, J. Ma and S. Fathpour, "High-contrast, all-silicon waveguiding platform for ultra-broadband mid-infrared photonics," *Applied Physics Letters* 103, no. 15, p. 151106, 2013.
- [19] J. Chiles and S. Fathpour, "Single-mode and single-polarization photonics with anchored-membrane waveguides," *Optics express* 24, no. 17, pp. 19337-19343, 2016.
- [20] J. Chiles and S. Fathpour, "Demonstration of ultra-broadband single-mode and single-polarization operation in T-Guides," *Optics letters* 41, no. 16, pp. 3836-3839, 2016.
- [21] P. Rabiei, J. Ma, S. Khan, J. Chiles and S. Fathpour, "Heterogeneous lithium niobate photonics on silicon substrates," *Optics express* 21, no. 21, pp. 25573-25581, 2013.

- [22] J. Chiles and S. Fathpour, "Mid-infrared integrated waveguide modulators based on silicon-on-lithium-niobate photonics," *Optica* 1, no. 5, pp. 350-355, 2014.
- [23] A. Rao, M. Malinowski, A. Honardoost, J. R. Talukder, P. Rabiei, P. Delfyett and S. Fathpour, "Second-harmonic generation in periodically-poled thin film lithium niobate wafer-bonded on silicon," *Optics express* 24, no. 26, pp. 29941-29947, 2016.
- [24] A. Rao, A. Patil, P. Rabiei, A. Honardoost, R. DeSalvo, A. Paoella and S. Fathpour, "High-performance and linear thin-film lithium niobate Mach-Zehnder modulators on silicon up to 50 GHz," *Optics letters* 41, no. 24, pp. 5700-5703, 2016.
- [25] A. Rao, J. Chiles, S. Khan, S. Toroghi, M. Malinowski, G. F. Camacho-González and S. Fathpour, "Second-harmonic generation in single-mode integrated waveguides based on mode-shape modulation," *Applied Physics Letters* 110, no. 11, p. 111109, 2017.
- [26] A. Rao and S. Fathpour, "Second-Harmonic Generation in Integrated Photonics on Silicon," *physica status solidi (a)* 215, no. 4, p. 1700684, 2017.
- [27] A. Rao and S. Fathpour, "Compact Lithium Niobate Electrooptic Modulators," *IEEE Journal of Selected Topics in Quantum Electronics* 24, no. 4, pp. 1-14, 2018.
- [28] J. Chiles, T. Sjaardema, A. Rao and S. Fathpour, "Damascene-patterned optical anisotropy in integrated photonics," *Optics Express* 25, no. 26, pp. 33664-33675, 2017.
- [29] G. Genty, S. Coen and J. M. Dudley, "Fiber supercontinuum sources," *JOSA B* 24, no. 8, pp. 1771-1785, 2007.
- [30] N. C. A. H. G. B. H. J. A. C. M. K. R. L. Petit, "Correlation between the nonlinear refractive index and structure of germanium-based chalcogenide glasses," *Materials Research Bulletin*, vol. 42, no. 12, pp. 2107-2116, 2007.

- [31] J. W. Choi, Z. Han, B.-U. Sohn, G. F. R. Chen, C. Smith, L. C. Kimerling, K. A. Richardson, A. M. Agrawal and D. T. H. Tan, "Nonlinear characterization of GeSbS chalcogenide glass waveguides," *Sci. Rep.*, vol. 6, p. 39234, 2016.
- [32] Y. Okawachi, M. R. Lamont, K. Luke, D. O. Carvalho, M. Yu, M. Lipson and A. L. Gaeta, "Bandwidth shaping of microresonator-based frequency combs via dispersion engineering," *Optics letters* 39, no. 12, pp. 3535-3538, 2014.
- [33] V. R. Almeida, Q. Xu, C. A. Barrios and M. Lipson, "Guiding and confining light in void nanostructure," *Optics letters* 29, no. 11, pp. 1209-1211, 2004.
- [34] J. Li, K. Xu and J. Du, "Ultrabroadband and Flattened Dispersion in Aluminum Nitride Slot Waveguides," *IEEE Photonics Journal* 9, no. 4, pp. 1-8, 2017.
- [35] L. Zhang, Q. Lin, Y. Yue, Y. Yan, R. G. Beausoleil and A. E. Willner, "Silicon waveguide with four zero-dispersion wavelengths and its application in on-chip octave-spanning supercontinuum generation," *Optics express* 20, no. 2, pp. 1685-169, 2012.
- [36] A. Harpin, P. Roscoe, A. G. Rickman, R. J. R. Morris and M. Asghar, "Tapered rib waveguide," *U.S. Patent 6,108,478*, 22 August 2000.
- [37] G. Stegeman, *Nonlinear Optics*, Wiley, 2012.
- [38] M. M. J.-E. T. A. R. G. F. C.-G. R. B. R. M. P. K. A. R. P. D. M. C. W. S. F. Saeed Khan, "Integrated thin-film lithium-niobate waveguides on silicon for second-harmonic generation pumped at 1875 nm.," *Conference on Lasers and Electro-Optics (CLEO) IEEE*, pp. 1-2, 2018.
- [39] R. Soref and J. Lorenzo, "All-silicon active and passive guided-wave components for  $\lambda = 1.3$  and  $1.6 \mu\text{m}$ ," *IEEE J. Quant. Elec.*, vol. 22, no. 6, p. 873-879, 1986.
- [40] J. Chiles and S. Fathpour, "Silicon photonics beyond silicon-on-insulator," *J. Opt.*, vol. 19, no. 5, p. 053001, 2017.

- [41] A. S. Mayer, A. Klenner, A. R. Johnson, K. Luke, M. R. E. Lamont, Y. Okawachi, M. Lipson, A. L. Gaeta and U. Keller, "Frequency comb offset detection using supercontinuum generation in silicon nitride waveguides," *Opt. Express*, vol. 23, no. 12, p. 15440–15451, 2015.
- [42] A. Klenner, A. S. Mayer, A. R. Johnson, K. Luke, M. R. E. Lamont, Y. Okawachi, M. Lipson, A. L. Gaeta and U. Keller, "Gigahertz frequency comb offset stabilization based on supercontinuum generation in silicon nitride waveguides," *Optics Express*, vol. 24, no. 10, pp. 11043–11053, 2016.
- [43] H. Jin, F. Liu, P. Xu, J. Xia, M. Zhong, Y. Yuan, J. Zhou, Y. Gong, W. Wang and S. Zhu, "On-Chip Generation and Manipulation of Entangled Photons Based on Reconfigurable Lithium-Niobate Waveguide Circuits," *Phys. Rev. Lett.*, vol. 113, no. 24, p. 103601, 2014.
- [44] Y.-K. Jiang and A. Tomita, "The generation of polarization-entangled photon pairs using periodically poled lithium niobate waveguides in a fibre loop," *J. Phys. B: At. Mol. Opt. Phys.*, 40, 437 (2007), vol. 40, no. 2, p. 437, 2007.
- [45] E. L. Wooten, K. M. Kissa, A. Yi-Yan, E. J. Murphy, D. A. Lafaw, P. F. Hallemeier, D. Maack, D. V. Attanasio, D. J. Fritz, G. J. McBrien and D. E. Bossi, "A review of lithium niobate modulators for fiber-optic communications systems," *IEEE J. Quant. Elec.*, vol. 6, no. 1, pp. 69–82, 2000.
- [46] J. L. Jackel, C. E. Rice and J. J. Veselka, "Proton exchange for high-index waveguides in LiNbO<sub>3</sub>," *Appl. Phys. Lett.*, vol. 41, no. 7, pp. 607–608, 1982.
- [47] L. Chang, M. H. P. Pfeiffer, N. Volet, M. Zervas, J. D. Peters, C. L. Manganelli, E. J. Stanton, Y. Li, T. J. Kippenberg and J. E. Bowers, "Heterogeneous integration of lithium niobate and silicon nitride waveguides for wafer-scale photonic integrated circuits on silicon," *Opt. Lett.*, vol. 42, no. 4, p. 803, 2017.
- [48] J.-E. Tremblay, Y.-H. Lin, M. N. Sakib, M. Malinowski, S. Novak, P. Qiao, C. Chang-Hasnain, K. Richardson, S. Fathpour and M. C. Wu, "High-Q and low-loss

chalcogenide waveguide for nonlinear supercontinuum generation," in *IEEE Photonics Conference*, 2016.

- [49] J. Chiles, M. Malinowski, A. Rao, S. Novak, K. Richardson and S. Fathpour, "Low-loss, submicron chalcogenide integrated photonics with chlorine plasma etching," *Appl. Phys. Lett.*, vol. 106, no. 11, p. 11110, 2015.
- [50] B. J. Eggleton, B. Luther-Davis and K. Richardson, "Chalcogenide photonics," *Nat. Photonics*, vol. 5, pp. 141-148, 2011.
- [51] F. Keilmann, C. Gohle and R. Holzwarth, "Time-domain mid-infrared frequency-comb spectrometer," *Opt. Lett.*, vol. 29, pp. 1542-1544, 2004.
- [52] C. F. Kaminski, R. S. Watt, A. D. Elder, J. H. Frank and J. Hult, "Supercontinuum radiation for applications in chemical sensing and microscopy," *Applied Physics B*, vol. 92, p. 367, 2008.
- [53] C. B. Huang, Z. Jiang, D. Leaird, J. Caraquitenia and A. Weiner, "Spectral line-by-line shaping for optical and microwave arbitrary waveform generations," *Laser Photonics Rev*, vol. 2, p. 227, 2008.
- [54] T. Steinmetz, T. Wilken, C. Araujo-Hauck, R. Holzwarth, T. W. Hänsch, L. Pasquini, A. Manescau, S. D'odorico, M. T. Murphy, T. Kentischer and W. Schmidt, "Laser frequency combs for astronomical observations," *Science*, vol. 321, p. 1335, 2008.
- [55] S. V. Smirnov, J. D. Ania-Castanon, T. J. Ellingham, S. M. Kobtsev, S. Kukarin and S. K. Turitsyn, "Optical spectral broadening and supercontinuum generation in telecom applications," *Optical Fiber Technology*, vol. 12, pp. 122-147, 2006.
- [56] T. J. Kippenberg, R. Holzwarth and S. A. Diddams, "Microresonator-based optical frequency combs," *Science*, vol. 332, pp. 555-559, 2011.
- [57] S. Miller, K. Luke, Y. Okawachi, J. Cardenas, A. L. Gaeta and M. Lipson, "On-chip frequency comb generation at visible wavelengths via simultaneous second- and third-order optical nonlinearities," *Opt. Express*, vol. 22, pp. 26517-26525, 2014.

- [58] K. Iwakuni, S. Okubo, O. Tadanaga, H. Inaba, A. Onae, F. L. Hong and H. Sasada, "Generation of a frequency comb spanning more than 3.6 octaves from ultraviolet to mid infrared," *Opt. Lett.*, vol. 41, pp. 3980-3983, 2016.
- [59] Y. Okawachi, M. Yu, J. Cardenas, X. Ji, M. Lipson and A. L. Gaeta, "Coherent, directional supercontinuum generation," *Opt. Lett.*, vol. 42, pp. 4466-4469, 2017.
- [60] M. R. E. Lamont, B. Luther-Davies, D. Y. Choi, S. Madden and B. J. Eggleton, "Supercontinuum generation in dispersion engineered highly nonlinear ( $\gamma = 10$  /W/m) As<sub>2</sub>S<sub>3</sub> chalcogenide planar waveguide," *Opt. Express*, vol. 16, pp. 14938-14944, 2008.
- [61] Y. Yu, X. Gai, P. Ma, D. Y. Choi, Z. Yang, R. Wang, S. Debbarma, S. J. Madden and B. Luther-Davies, "A broadband, quasi-continuous, mid-infrared supercontinuum generated in a chalcogenide glass waveguide," *Laser Photonics Rev.*, vol. 8, p. 792-798, 2014.
- [62] M. A. Ettabib, L. Xu, A. Bogris, A. Kapsalis, M. Belal, E. Lorent, P. Labeye, S. Nicoletti, K. Hammani, D. Syvridis, D. P. Shepherd, J. H. V. Price, D. J. Richardson and P. Petropoulos, "Broadband telecom to mid-infrared supercontinuum generation in a dispersion-engineered silicon germanium waveguide," *Opt. Lett.*, vol. 40, no. 17, pp. 4118-4121, 2015.
- [63] U. D. Dave, C. Ciret, S. P. Gorza, S. Combrie, A. D. Rossi, F. Raineri, G. Roelkens and B. Kuyken, "Dispersive-wave-based octave-spanning supercontinuum generation in InGaP membrane waveguides on a silicon substrate," *Opt. Lett.*, vol. 40, pp. 3584-3587, 2015.
- [64] N. Singh, M. Xin, D. Vermeulen, K. Shtyrkova, N. Li, P. T. Callahan, E. S. Magden, A. Ruocco, N. Fahrenkopf, C. Baiocco, B. P. P. Kuo, S. Radic, E. Ippen, F. X. Kärtner and M. R. Watts, "Octave-spanning coherent supercontinuum generation in silicon on insulator from 1.06  $\mu\text{m}$  to beyond 2.4  $\mu\text{m}$ ," *Light: Science & Applications*, vol. 7, p. 17131, 2018.

- [65] M. A. G. Porcel, F. Schepers, J. P. Epping, T. Hellwig, M. Hoekman, R. G. Heideman, P. J. M. v. d. Slot, C. J. Lee, R. Schmidt, R. Bratschitsch, C. Fallnich and K. J. Boller, "Two-octave spanning supercontinuum generation in stoichiometric silicon nitride waveguides pumped at telecom wavelengths," *Opt. Exp.*, vol. 25, no. 2, pp. 1542-1554, 2017.
- [66] D. D. Hickstein, H. Jung, D. R. Carlson, A. Lind, I. Coddington, K. Srinivasan, G. G. Ycas, D. C. Cole, A. Kowligy, C. Fredrick, S. Droste, E. S. Lamb, N. R. Newbury, H. X. Tang, S. A. Diddams and S. B. Papp, "Ultrabroadband supercontinuum generation and frequency-comb stabilization using on-chip waveguides with both cubic and quadratic nonlinearities," *Phys. Rev. Applied*, vol. 8, p. 014025, 2017.
- [67] A. Honardoost, G. F. Camacho-Gonzalez, S. Khan, M. Malinowski, A. Rao, J. E. Tremblay, A. Yadav, K. A. Richardson, M. C. Wu and S. Fathpour, "Cascaded integration of optical waveguides with third-order nonlinearity with lithium niobate waveguides on silicon substrates," *IEEE Photonics Journal*, vol. 10, no. 3, pp. 1-9, 2018.
- [68] S. Roy, S. K. Bhadra and G. P. Agrawal, "Effects of higher-order dispersion on resonant dispersive waves emitted by solitons," *Opt. Lett.*, vol. 34, pp. 2072-2074, 2009.
- [69] S. Roy, D. Ghosh, S. K. Bhadra and G. P. Agrawal, "Role of dispersion profile in controlling emission of dispersive waves by solitons in supercontinuum generation," *Optics Communications*, vol. 283, pp. 3081-3088, 2010.
- [70] G. P. Agrawal, *Nonlinear fiber optics*, California, USA: Academic Press, 2001.
- [71] G. Ghosh, M. Endo and T. Iwasaki, "Temperature-dependent Sellmeier coefficients and chromatic dispersions for some optical fiber glasses," *Journal of Lightwave Technology*, vol. 12, pp. 1338-1342, 1994.
- [72] J. E. Tremblay, M. Malinowski, K. A. Richardson, S. Fathpour and M. C. Wu, "Picojoule-level octave-spanning supercontinuum generation in chalcogenide waveguides," *Opt. Express*, vol. 26, pp. 21358-21363, 2018.

- [73] D. E. Zelmon, D. L. Small and D. Jundt, "Infrared corrected Sellmeier coefficients for congruently grown lithium niobate and 5 mol. % magnesium oxide-doped lithium niobate," *J. Opt. Soc. Am. B*, vol. 14, pp. 3319-3322, 1997.
- [74] I. H. Malitson, "Interspecimen comparison of the refractive index of fused silica," *Josa*, vol. 55, pp. 1205-1209, 1965.
- [75] H. Saghaei, M. Moravvej-Farshi, M. Ebnali-Heidari and M. Moghadasi, "Ultra-wide mid-infrared supercontinuum generation in As<sub>40</sub>Se<sub>60</sub> chalcogenide fibers: Solid core PCF versus SIF," *IEEE Selected Topics in Quantum Electronics*, vol. 20, pp. 279-286, 2016.
- [76] J. M. Dudley, G. Genty and S. Coen, "Supercontinuum generation in photonic crystal fiber," *Reviews of Modern Physics*, vol. 78, p. 1135, 2006.
- [77] C. Goncalves, M. Kang, B.-U. Sohn, G. Yin, J. Hu, D. Tan and K. Richardson, "New candidate multicomponent chalcogenide glasses for supercontinuum generation," *Applied Sciences*, vol. 8, p. 2082, 2018.
- [78] V. S. Afshar, T. M. Monroe and C. M. d. Sterke, "Understanding the contribution of mode area and slow light to the effective Kerr nonlinearity of waveguides," *Opt. Express*, vol. 21, pp. 18558-18571, 2013.
- [79] J. M. Dudley, L. Provino, N. Grossard, H. Maillotte, R. S. Windeler, B. J. Eggleton and S. Coen, "Supercontinuum generation in air-silica microstructured fibers with nanosecond and femtosecond pulse pumping," *J. Opt. Soc. Am. B*, vol. 19, pp. 765-771, 2002.
- [80] S. Fathpour, "Heterogeneous Nonlinear Integrated Photonics.," *IEEE Journal of Quantum Electronics*, vol. 54, no. 6, pp. 1-16, 2018.